UNIVERSITY OF ALBERTA
LIBRARY RELEASE FORM

NAME OF AUTHOR:	Fredric Kalen Martens
TITLE OF THESIS:	Elastic Production and Decay of Rho Mesons at HERMES
DEGREE:	Master of Science
YEAR THE DEGREE GRANTED:	1998

Fredric Kalen Martens
Department of Physics
University of Alberta
Edmonton, Alberta
T6G 2J1

Date:

Whoever undertakes to set himself up as judge in the field of truth and knowledge is shipwrecked by the laughter of the Gods.

ALBERT EINSTEIN

University of Alberta

Elastic Production and Decay of Rho Mesons at HERMES

By

Fredric Kalen Martens

A dissertation

presented to the Faculty of Graduate Studies and Research

in partial fulfilment of the requirements for the degree

of

Master of Science

Department of Physics

Edmonton, Alberta

Spring 1998

UNIVERSITY OF ALBERTA

FACULTY OF GRADUATE STUDIES AND RESEARCH

The undersigned certify that they have read, and recommend to the Faculty of Graduate Studies and Research for acceptance, a thesis entitled "Elastic Production and Decay of Rho Mesons at HERMES" submitted by Fredric Kalen Martens in partial fulfilment of the requirements for the degree of Master of Science.

Prof. P. Kitching Supervisor

Prof. L.G. Greeniaus

Prof. J.S. Schaeffer

Date:

Prof. J. Beamish

Abstract

The Vector Dominance Model (VDM) contends that the photon spends part of the time as quark-antiquark pairs, and specifically as one of the vector mesons. This makes it possible for a virtual photon (γ^*) to interact strongly with a nuclear target and for real ρ^0 mesons to be produced. The subsequent decay of the ρ^0 meson ($\rho^0 \to \pi^+\pi^-$) can give important information regarding this interaction. In particular, the physics of how the spin is transferred in the $\gamma^* - \rho^0$ system can be studied. A few thousand elastically produced ρ^0 mesons are available for analysis in the 1995 data from the HERMES experiment. The theory and physics of ρ^0 production will be presented, as well as an overview of the HERMES spectrometer. Results of the study will also be presented and compared to the results of other experiments.

Acknowledgements

I would like to take this opporunity to thank everyone who has made the last two years (or so) an educational experience for me. I have learned alot from my involvement with HERMES.

I would be negligent if I did not at the very least thank Eric Belz from whom I have learned the most. My frequent contact with him was a major factor in making this thesis possible.

I especially would like to thank my supervisor, Peter Kitching, for his guidance, support, and his patience.

I know I may never see many of the people that I have come to know in the last two years ever again. I would like to wish everyone all the best for now and in the future.

Contents

List of Tables

List of Figures

CHAPTER 1

Introduction

It has been known for some time that matter can be converted to energy and *vice versa*. Colliding particles together at high enough energies allows the possibility for the creation of new particles. One of the major aims of the field of subatomic physics is to study the creation and properties of these particles. Both small and large machines have been built to accelerate particles such as electrons, positrons, protons, etc. in a beam to high energies and collide them with a target. In some cases, beams of particles travelling in the opposite direction are collided together. To "see" what results from these collisions, detectors have also been designed and constructed. The type of particle accelerated, the energy obtained, the type of target used, and the design of the detector are specific to the particular physics problem that is under investigation. As a result, there are numerous accelerators and detectors in existence today.

The collection of theories that describes all matter and its interactions is known as the Standard Model. In this model, there are six types of quarks and six types of leptons in three generations and are listed in Table 1.1. Each quark (q) has a corresponding antiparticle: an antiquark ($\overline{q}$) of opposite charge. Similarily, each of the leptons also has an associated antiparticle; the antiparticle of the electron (e^-) is the positron (e^+), for example. A property that the quarks and leptons have in common is that they possess an intrinsic angular momentum (spin) of magnitude $\frac{1}{2}\hbar$.

There are four forces in nature that govern the interactions of the quarks and

Generation	Quarks			Leptons		
	Name	Symbol	Charge	Name	Symbol	Charge
1st generation	down	d	$-\frac{1}{3}$	electron	e^-	-1
	up	u	$+\frac{2}{3}$	electron neutrino	ν_e	0
2nd generation	strange	s	$-\frac{1}{3}$	muon	μ^-	-1
	charm	c	$+\frac{2}{3}$	muon neutrino	ν_μ	0
3rd generation	bottom	b	$-\frac{1}{3}$	tau	τ^-	-1
	top	t	$+\frac{2}{3}$	tau neutrino	ν_τ	0

Table 1.1: The three generations of quarks and leptons. The quarks are ordered from lightest to heaviest with d being the lightest quark.

leptons. The weakest of these is the familiar gravitational force and is not included as part of the Standard Model. The other forces are the electromagnetic force and the strong and weak forces. These forces arise from the exchange of another class of particles called bosons. For the electromagnetic force, the boson is the photon and is exchanged between charged particles. The theory of electromagnetic interactions is *quantum electrodynamics* (QED). The weak force can be responsible for the interaction of both quarks and leptons and is mediated by three particles called the Z^0, W^+, W^-. QED and the theory of the weak interactions have been combined into a single *electroweak* theory. Gluons are the bosons responsible for the strong force which is described by *quantum chromodynamics* (QCD). The bosons all have an intrinsic angular momentum of $1\hbar$.

Quarks must exist in bound states with other quarks or antiquarks and only certain combinations are allowed. Baryons contain three quarks (qqq), anti-baryons contain three antiquarks ($\overline{q}\,\overline{q}\,\overline{q}$), and mesons are made of a quark and antiquark. Familiar examples of baryons are the proton and neutron. The lightest mesons are pions. Particles composed of quarks are collectively known as *hadrons*. The actual situation is not quite as simple as this, however, because hadrons contain much more than two or three quarks. Gluons are continuously exchanged between the quarks as the mediators of the strong force. As well, quark-antiquark pairs can appear for short times as permitted by the Heisenberg uncertainty principle and are known as sea quarks. Because the quarks in the combinations listed above are always present, they are referred to as the valence quarks. Also, quarks and gluons are collectively known as *partons*.

In addition to electric charge, quarks also possess one of the color charges, designated blue, red, and green. All of the above quark combinations (baryons, anti-baryons, and mesons) have a total color charge of zero. Particles with a net color charge, including free quarks, are not found in nature. Quarks are therefore confined in bound states inside of baryons and mesons and this notion is known as quark confinement.

As described above, it is believed that QCD describes the strong interactions. However, the large value of the strong coupling constant makes calculations in this theory very hard to do. In fact, the coupling constant increases as distances between color charged quarks increase. As a result, perturbative solutions in QCD are not possible at low energies. Experimental measurements are therefore important as a guide to and confirmation of theoretical calculations.

The physics that will be investigated concerns a particle called the ρ^0 meson. It is termed a vector meson which means that it possesses an intrinsic angular momentum of $1\hbar$ and consists of a quark-antiquark ($q\overline{q}$) pair. More specifically, the ρ^0 is a linear superposition of the up–anti-up ($u\overline{u}$) and down–anti-down ($d\overline{d}$) valence quark states:

$$| \rho^0 >= \frac{1}{\sqrt{2}}[| u\overline{u} > - | d\overline{d} >]. \tag{1.1}$$

The ρ^0 meson is produced in the HERMES experiment when high energy positrons are scattered from a target of ^{3}He gas.

In lepton scattering experiments, there are two ways in which the ρ^0 may be produced. In both cases, a virtual photon (γ^*) emitted by the incident lepton interacts with the target. A virtual photon differs from a real photon in that it does not have zero mass and can only travel short distances. The virtual photon may exist for short periods of time as $q\overline{q}$ pairs as permitted by the Heisenberg uncertainty principle, and in particular, as one of the vector mesons. This is known as the Vector Dominance Model (VDM) [1]. A real vector meson can be produced when the $q\overline{q}$ pair interacts via the strong force with the target. See Figure 1.1. This is known as the *elastic* leptoproduction of vector mesons.

The second way that ρ^0 mesons can be produced is when the virtual photon is absorbed by one of the constituent quarks of the target nucleus. This can happen if the wavelength of the virtual photon is small enough to "see" the individual quarks rather than the whole nucleon or nucleus and is referred to as deep inelastic scattering (DIS). The QCD requirement that no free quarks exist in nature means that $q\overline{q}$ pairs are produced in the color field created as the struck quark tries to leave the confines of the nucleus. This process is known as fragmentation and, most any type of particle can be created in this way, including the ρ^0 meson which has relatively low mass.

The strong force is responsible for the decay of the ρ^0. A characteristic of particles that decay via the strong interaction is that they have very short lifetimes. A ρ^0 meson at rest has a lifetime of $\sim 10^{-24}$ s. Even at energies of a few GeV, the ρ^0 does not travel much farther than the width of a nucleus before it decays. The predominant decay mode is into two pions ($\rho^0 \rightarrow \pi^+\pi^-$) which happens $\sim 100\%$ of the time [2]. Although the pions themselves decay into other particles, their lifetime

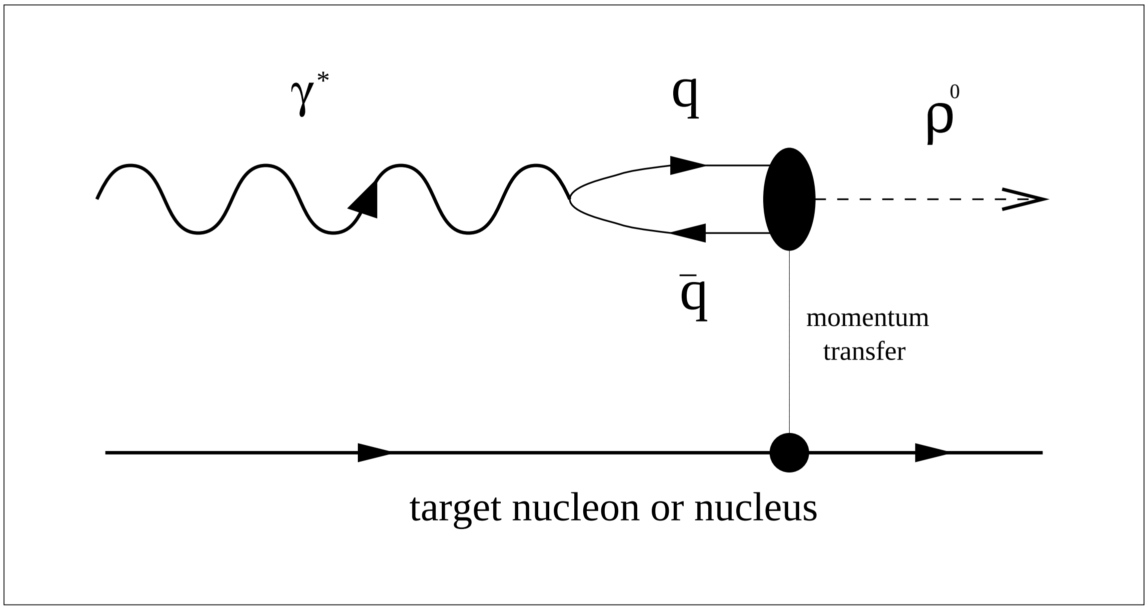

Figure 1.1: Production of a ρ^0 meson in the Vector Dominance Model. A virtual photon exists briefly as a $q\overline{q}$ pair and scatters from a nuclear target to become a real ρ^0 meson.

is long enough that they are able to travel some distance. In the case that will be considered, the pions are the particles that are observed and most of them travel through the spectrometer ($\sim$ 8 m) before they decay.

When the two pions are detected and their momenta determined, the ρ^0 meson's momentum, energy, and mass can be calculated. Information about the helicity of the ρ^0 can also be found by examining the polar and azimuthal distributions of the pions in a large number of decays. The helicity of a particle is the component of its spin in the direction of its motion. For a particle with a spin of $1\hbar$, the possible values of helicity that it can have are -1, 0, and $+1$. The only exception is for a massless particle such as a real photon where the possible values are limited to -1 and $+1$. The reason lies in the theory of relativity and the fact that the photon travels at the speed of light. However, the ρ^0 meson and the virtual photon are not massless particles and can possess a helicity value of 0.

The physics of interest is the relationship between the helicities of the virtual photons and elastically produced ρ^0s. The angular distributions of the decay depend on the helicity of the ρ^0. Likewise, the kinematics of the scattered lepton gives the helicity state of the γ^*. The details of how these helicity states are related are the subject of Chapter 2. This information can yield insights on the nature of elastic ρ^0 production as well as on the nature of the interaction of the $q\overline{q}$ system with the target. S-channel helicity conservation (SCHC) is a model in which the helicity of the ρ^0 is the same as the helicity of the virtual photon – this model will be assumed. The analysis will be concerned with showing that SCHC is consistent with the data.

A few thousand elastically produced ρ^0 mesons have been found in the HERMES data of 1995 and are the subject of this thesis. The formalism of elastic ρ^0 production and the interpretation of the resulting angular distributions will be presented in Chapter 2 of this thesis. Chapter 3 will provide an overview of the positron beam, the ^{3}He target, and the HERMES spectrometer. A description of the Monte Carlo simulation of the spectrometer will be given in Chapter 4 as it plays an important role in the analysis. The analysis of the data will be discussed in Chapter 5. Issues of concern will be the extraction of candidate events, the optimization of cuts on kinematic variables, background and acceptance.

The Heaviside-Lorentz system of units will be used throughout this thesis. In this system, the value for the speed of light, c, and the unit for angular momentum, $\hbar$, are equal to 1. The exception will be in cases where the inclusion of these units makes the explanation or argument being made more clear.

CHAPTER 2

Elastic ρ^0 Production

In deep inelastic scattering (DIS), the production of the ρ^0 vector meson is thought to arise from fragmentation processes. Specifically, the virtual photon strikes a single quark and, as a result of colour confinement, quark-antiquark pairs are produced with the possibility of producing a ρ^0. A model which embodies this idea will be outlined in Chapter 4 when the Monte Carlo that simulates HERMES physics is discussed.

There is another, different, mechanism by which ρ^0 mesons can be created. The Heisenberg uncertainty principle allows a photon to exist for short times as quark-antiquark pairs and specifically as the vector mesons ρ^0, ω^0, ϕ^0 when only the light quarks (u,d,s) are considered. Since, the vector mesons have the same quantum numbers as the photon, the real photon state can be written as the following superposition of states:

$$|\,\gamma >_{real} = \ a\,|\,\gamma >_{bare} + \sum_{h=\rho^0,\omega^0,\phi^0} b_h\,|\,h>, \tag{2.1}$$

where $|\,\gamma >_{bare}$ represents the pure electromagnetic part and $|\,h>$ represents the hadronic component of the real photon. The constants a and b_h are included in the formula for normalization. This concept is known as the Vector Dominance Model (VDM)[1]. Because the photon has a non-zero hadronic content, a strong interaction of the photon with the target nucleus becomes possible in which the vector meson

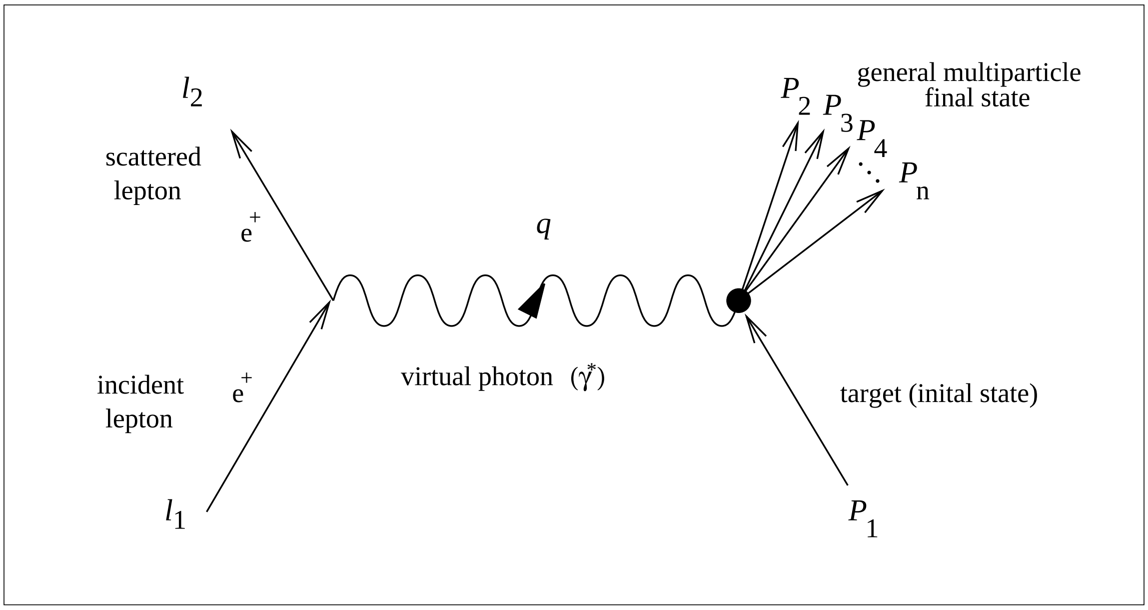

Figure 2.1: Diagram and kinematical definitions for a general DIS event.

can be scattered onto its mass shell. This mechanism is is referred to as *elastic* vector meson production in the modern literature.

After a preliminary description of the kinematics and some useful coordinate systems, the general formalism for elastic ρ^0 leptoproduction and decay distributions will be outlined in this chapter. A great deal of this chapter's content is based on [3].

2.1 Kinematics

In a deep inelastic scattering event, the target may undergo fragmentation and result in a final state with one or more particles. A general diagram of a DIS event for lowest order in QED is shown in Figure 2.1. The 4-momenta of the incident and scattered positron are l_1 and l_2, respectively, P_1 is the 4-momentum of the target nucleon, and q is the 4-momentum of the virtual photon.

The 4-momenta are four component vectors where the first component is the energy of the particle and the remaining three are the x, y, and z components of the usual momentum vector. The components of the 4-momentum are normally numbered from 0 to 3. Squaring the 4-momentum of a particle gives the square of the rest mass of that particle. For example, if $(E, \vec{p})$ is the 4-momentum for a particle of mass M, then

$$M = \sqrt{E^2 - |\vec{p}|^2}. \tag{2.2}$$

Letting P' be the vector sum of the 4-momenta of the particles that emerge from the γ^*–target interaction shown in Figure 2.1,

$$P' = P_2 + P_3 + ... + P_n \,, \tag{2.3}$$

the following Lorentz invariants can be defined

$$Q^2 = -q^2 = -(l_1 - l_2)^2 \tag{2.4}$$

$$\nu = \frac{p \cdot q}{M_{targ}} \tag{2.5}$$

$$W^2 = P'^2 = M_{targ}^2 + 2M_{targ}\nu - Q^2, \tag{2.6}$$

where M_{targ} is the mass of the target. In the lab frame, Q^2 and ν can be calculated as

$$Q^2 \overset{\text{lab}}{\simeq} 4EE' \sin^2(\frac{\theta_{lab}}{2}) \tag{2.7}$$

$$\nu \overset{\text{lab}}{=} E - E' \tag{2.8}$$

and ν becomes the energy of the virtual photon. The angle θ_{lab} is the positron scattering angle in the lab frame. The variables E and E' are the energies in the lab frame of the incident and scattered positron, respectively. The calculation of Q^2 in the lab frame uses the approximation that E and E' are much larger than the positron mass, m.

Another useful quantity, y, is given by

$$y = \frac{\nu}{E} \overset{\text{lab}}{=} \frac{E - E'}{E} \tag{2.9}$$

and represents the fraction of virtual photon energy to the energy of the incident positron when evaluated in the lab frame. All of these definitions are summarized in Table 2.1.

The process of interest is the elastic leptoproduction of the ρ^0 vector meson

$$e^+ N \longrightarrow e^{+'} \rho^0 N'. \tag{2.10}$$

In contrast to the DIS case, the target in both the initial and final states (N and N') will be the same particle. The kinematics for this case are shown in Figure 2.2. Here, P_2 is the 4-momentum of the target in the final state and v is the 4-momentum of the ρ^0 meson.

The 4-momentum of the ρ^0 will be the sum of the 4-momenta of the pions (p_{π^+}, p_{π^-}) from its decay

$$v = p_{\pi^+} + p_{\pi^-} \tag{2.11}$$

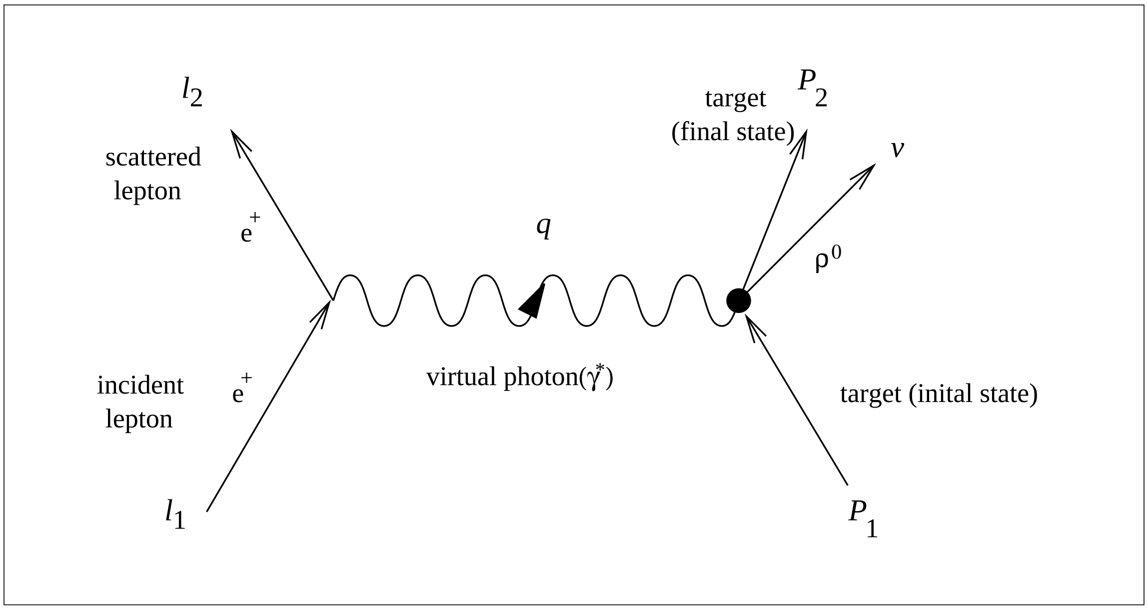

Figure 2.2: Kinematical definitions of ρ^0 leptoproduction in the single photon approximation.

and the mass of the ρ^0 meson, M_{ρ^0}, can then be found with the equation

$$M_{\rho^0} = \sqrt{(E_{\pi^+} + E_{\pi^-})^2 - \mid \vec{p}_{\pi^+} + \vec{p}_{\pi^-} \mid^2}\,. \tag{2.12}$$

Elastic ρ^0 production has characteristics of diffractive scattering and is commonly referred to as *diffractive* ρ^0 production. Part of the reason is that the cross section falls off exponentially with t,

$$\frac{d\sigma}{dt} \sim e^{-b|t|}, \tag{2.13}$$

where t is the momentum transfer to the target and is defined as $t = (q - v)^2$. The variable b is related to the size of the target. Other characteristics of a diffractive process include a cross section that is nearly energy independent and s-channel helicity conservation [4]. Also, some older literature describes this process as *inelastic* ρ^0

production which reflects the fact that a particle was created. A variable related to t is also commonly defined. It is given as

$$t' = t - t_{min} \tag{2.14}$$

where t_{min} is just t in the limit where the angle between $\vec{q}$ and $\vec{v}$ goes to zero in the γ^*–ρ^0 center of momentum (c.m.) frame and is given by

$$t_{min} = M_{\rho^0}^2 - Q^2 + 2(|\vec{q}_{cm}||\vec{v}_{cm}| - E_{\rho^0 cm}\nu). \tag{2.15}$$

The notation used is standard but can be somewhat confusing since $t_{min} > t$.

The scattered target is usually not detected in an experiment. The invariant mass of this undetected final state can be calculated and compared to the original target mass to determine if elastic production did indeed take place. If it is assumed that the two detected hadrons are pions as a result of ρ^0 decay, the mass of the undetected hadronic state, M_X, can be calculated as

$$M_X = \sqrt{(q + P_1 - v)^2}\,. \tag{2.16}$$

A measure of the difference in mass is given by

$$\Delta E = \frac{(M_X^2 - M_{targ}^2)}{2M_{targ}} \tag{2.17}$$

and should be close to zero for elastic ρ^0 production.

Table 2.1 summarizes the kinematical variables typically used to describe ρ^0 leptoproduction and DIS events.

Variable	Equation and Description
l_1, l_2	4-momenta of the incoming and scattered positron, respectively. $l_1 = (E, \vec{l_1})$, $l_2 = (E', \vec{l_2})$
m	Mass of the positron, $m = 0.511$ MeV.
q	4-momenta of the virtual photon. $q = l_1 - l_2$
ν	Energy of the virtual photon (in the lab frame). $\nu = (p \cdot q)/M_{targ} \overset{\text{lab}}{=} (E - E')$
y	Fraction of E possessed by the virtual photon (in the lab frame). $y = \nu/E \overset{\text{lab}}{=} (E - E')/E$
Q^2	Negative of the 4-momenta squared of the virtual photon. $Q^2 = -q^2 = -(l_1 - l_2)^2$
P_1, P_2	4-momenta of the target in the initial and final state, respectively. $P_1 = (M_{targ}, 0)$
v	4-momenta of the ρ^0. $v = p_{\pi^-} + p_{\pi^-} = (E_{\rho^0}, \vec{v})$
t	Square of the momentum transfer to the target. $t = (q - v)^2$
t_{min}	t in the limit where the angle between $\vec{q}$ and $\vec{v}$ goes to zero in the γ^*–ρ^0 c.m. frame. $t_{min} = M_{\rho^0}^2 - Q^2 + 2(\lvert\vec{q}_{cm}\rvert\lvert\vec{v}_{cm}\rvert - E_{\rho^0 cm}\nu)$
t'	Alternative measure of t. $t' = t - t_{min}$
W^2	Invariant mass of the total hadronic final state. $W^2 = (q + P_1)^2$
M_X	Mass of the undetected hadronic final state. $M_X = \sqrt{(q + P_1 - v)^2}$
ΔE	Measure of mass difference between M_{targ} and M_X. $\Delta E = (M_X^2 - M_{targ}^2)/2M_{targ}$
M_{ρ^0}	Invariant mass of the ρ^0. $M_{\rho^0} = \sqrt{(E_{\pi^+} + E_{\pi^-})^2 - \mid \vec{p}_{\pi^+} + \vec{p}_{\pi^-} \mid^2}$

Table 2.1: Definitions of kinematic variables related to elastic ρ^0 production and deep inelastic scattering.

2.2 Coordinate Systems

It is useful to introduce the following orthonormal coordinate system in the hadronic center of momentum (c.m.) frame,

$$\vec{Z} = \frac{\vec{q}^{\,*}}{\mid \vec{q}^{\,*} \mid}, \quad \vec{Y} = \frac{\vec{q}^{\,*} \times \vec{v}^{\,*}}{\mid \vec{q}^{\,*} \times \vec{v}^{\,*} \mid}, \quad \vec{X} = \vec{Y} \times \vec{Z}. \tag{2.18}$$

Here, the Z-axis is in the direction of the momentum of the virtual photon, $\vec{q}^{*}$, and the Y-axis is perpendicular to the plane defined by $\vec{q}^{*}$ and $\vec{v}^{*}$ (see Figure 2.3) where the asterisks for superscripts indicate that the corresponding vectors are taken in the hadronic c.m. frame. (The standard notation for the virtual photon in any frame is γ^{*} and should not be confused with these vectors.) The angle θ_V^{*} is the angle between $\vec{q}^{\,*}$ and $\vec{v}^{\,*}$ in this frame,

$$\cos \theta_V^{*} = \frac{\vec{q}^{\,*} \cdot \vec{v}^{\,*}}{\mid \vec{q}^{\,*} \mid\mid \vec{v}^{\,*} \mid} \,. \tag{2.19}$$

The angle, Φ, in Figure 2.3 is the angle between the normals of the ρ^0 production plane, $\vec{Y}$, and the lepton scattering plane, $(\vec{l}_1^{*} \times \vec{l}_2^{*}) / \mid \vec{l}_1^{*} \times \vec{l}_2^{*} \mid$.

The decay angular distributions are examined in the helicity system of the rest frame of the ρ^0 (see Figure 2.4). This frame is obtained by a boost in the direction of $\vec{v}^{*}$ in Figure 2.3. The z-axis in this frame is in the opposite direction to the outgoing nucleus and the y-direction is the same direction as $\vec{Y}$ above,

$$\vec{z} = \frac{-\vec{n}_2^{*}}{\mid \vec{n}_2^{*} \mid}, \quad \vec{y} = \vec{Y}, \quad \vec{x} = \vec{y} \times \vec{z}. \tag{2.20}$$

The decay distributions are described by the direction of the positive pion in the ρ^0

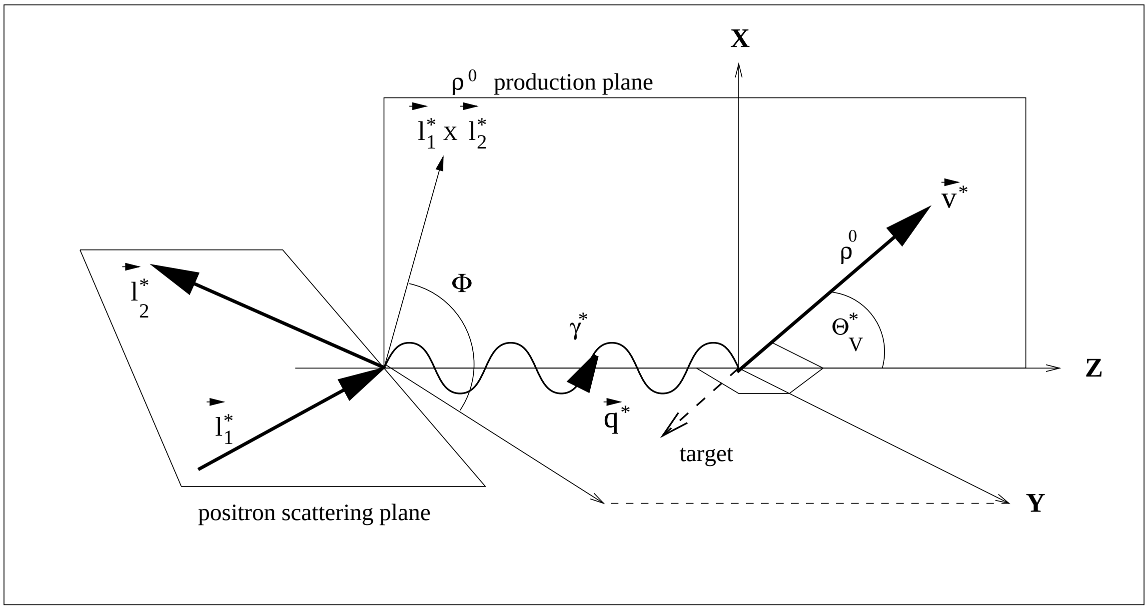

Figure 2.3: Definition of the coordinate system in the hadronic c.m. frame

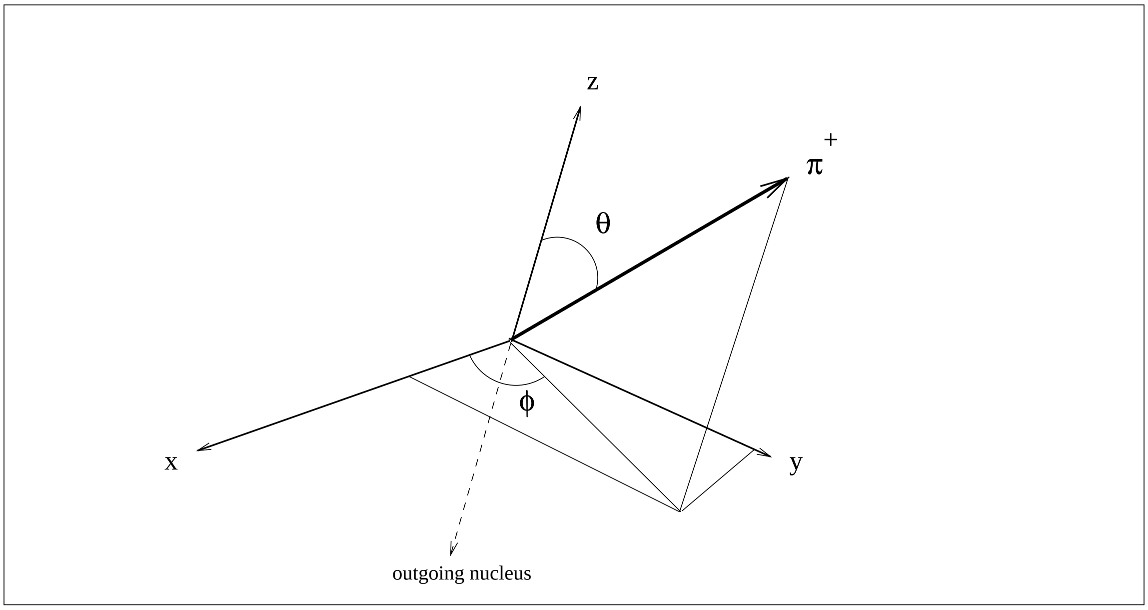

Figure 2.4: Definition of the coordinate system in the rest frame of the helicity system of the ρ^0.

rest frame and are defined by the polar and azimuthal angles θ and ϕ, respectively.

2.3 Spin Density Matrices

The differential cross section for diffractive ρ^0 production is given by [3]

$$\frac{d\sigma}{dE'd\Omega d\Phi dt} = \frac{1}{(2\pi)^5}\frac{E'}{E}\frac{m^2}{4(\nu^2+Q^2)^{1/2}}\frac{1}{Q^4}\frac{1}{4}\sum_{spins} \mid \mathcal{M} \mid^2, \tag{2.21}$$

where $d\Omega$ is the solid angle into which the positron is scattered. The angle Φ is the angle between the normals of the ρ^0 production plane and the positron scattering plane as defined in the last section.

The squared magnitude of the matrix element can be written as

$$\mid \mathcal{M} \mid^2 = \frac{e^4}{m^2}\lambda_{\mu\nu}t^{\mu\nu}, \tag{2.22}$$

where

$$\lambda_{\mu\nu} = m^2 < \ell_2 | \, j^{el}_{\mu} \mid \ell_1 >< \ell_2 | \, j^{el}_{\nu} \mid \ell_1 >^* \tag{2.23}$$

$$t^{\mu\nu} =< n_2 v | \, j^{el\,\mu} \mid n_1 >< n_2 v | \, j^{el\,\nu} \mid n_1 >^* . \tag{2.24}$$

The states $\mid \ell_1 >$ and $\mid \ell_2 >$ represent the initial and final state of the positron, respectively. Similarily, $\mid n_1 >$ represents the initial state of the target and $\mid vn_2 >$ is the hadronic final state that includes both the scattered target and vector meson.

The case for unpolarized positrons can be treated by summing $\lambda_{\mu\nu}$ over the initial and averaging over the final lepton spin states. By elimination of the scalar component using current conservation, the spin density matrix of the virtual photon, $\rho(\gamma^*)_{unpol}$, can be obtained [3]. In the hadronic c.m. frame and assuming $Q^2 \gg m^2$, it is written as

$$\rho(\gamma^*)_{unpol} = \frac{1}{2}\begin{bmatrix} 1 & \sqrt{\epsilon(1+\epsilon)}e^{-i\Phi} & -\epsilon e^{-2i\Phi} \\ \sqrt{\epsilon(1+\epsilon)}e^{i\Phi} & 2\epsilon & -\sqrt{\epsilon(1+\epsilon)}e^{-i\Phi} \\ -\epsilon e^{2i\Phi} & -\sqrt{\epsilon(1+\epsilon)}e^{i\Phi} & 1 \end{bmatrix}, \qquad (2.25)$$

where ϵ, the polarization parameter evaluated in the lab frame, is given by

$$\epsilon \simeq \left[1 + \frac{2(Q^2+\nu^2)}{Q^2}\tan^2(\frac{\theta_{lab}}{2})\right]^{-1}, \quad (Q^2 \gg m^2). \qquad (2.26)$$

The indicies of the elements of $\rho(\gamma^*)_{unpol}$ correspond to the possible helicities that the virtual photon can possess: $+1$, 0, and -1.

In the case where the polarization of the incident leptons is measured, the virtual photon spin density matrix is modified with the addition of the matrix [3] $(Q^2 \gg m^2)$

$$\rho(\gamma^*)_{pol} = \frac{P\sqrt{1-\epsilon}}{2}\begin{bmatrix} \sqrt{1+\epsilon} & \sqrt{\epsilon}e^{-i\Phi} & 0 \\ \sqrt{\epsilon}e^{i\Phi} & 0 & \sqrt{\epsilon}e^{-i\Phi} \\ 0 & \sqrt{\epsilon}e^{i\Phi} & -\sqrt{1+\epsilon} \end{bmatrix} \qquad (2.27)$$

where P is the degree of longitudinal polarization of the incident positrons. This matrix will be added to (subtracted from) $\rho(\gamma^*)_{unpol}$ if the spins of the positrons are parallel (anti-parallel) to the momentum of the beam.

Matrix	Polarization
Σ^0	unpolarized
Σ^1, Σ^2	linear
Σ^3	circular
Σ^4	longitudinal
Σ^5–Σ^8	longitudinal/transverse interference

Table 2.2: Polarization components of the spin density matrices.

The photon density matrix, $\rho(\gamma^*) = \rho(\gamma^*)_{unpol} + \rho(\gamma^*)_{pol}$, can be written as a linear combination of an orthogonal set of Hermitian matrices, Σ^α $(\alpha = 0 - 8)$,

$$\rho(\gamma^*) = \sum_{\alpha=0}^{8} \tilde{\Pi}_\alpha \Sigma^\alpha. \tag{2.28}$$

The Σ^α matrices correspond to the various polarization components of the virtual photon as described in Table 2.2. They are explicitly written out in Appendix A. A spin-1 particle with helicity equals 0 is said to be longitudinally polarized.

The spin density matrix of the ρ^0 vector meson, $\rho(V)$, is related to $\rho(\gamma^*)$ by

$$\rho(V) = \frac{1}{2} T \rho(\gamma^*) T^\dagger \tag{2.29}$$

where the T are (helicity) amplitudes connecting the various helicity states of the ρ^0 and virtual photon.

The spin density matrix for the ρ^0 can also be written in a form similar to (2.28)

$$\rho(V) = \sum_{\alpha=0}^{8} \Pi_\alpha \rho^\alpha \, . \tag{2.30}$$

Using Eqns. 2.28 and 2.29, it can be shown that terms of the Σ^{α}, the $\rho^{\alpha}_{\lambda_V \lambda'_V}$ are given as [3]

$$\rho^{\alpha}_{\lambda_V \lambda'_V} = \frac{1}{2N_{\alpha}} \sum_{\lambda_{N'} \lambda_N \lambda_{\gamma} \lambda'_{\gamma}} T_{\lambda_V \lambda_{N'} \lambda_{\gamma} \lambda_N} \Sigma^{\alpha}_{\lambda_{\gamma} \lambda'_{\gamma}} T^{*}_{\lambda_V \lambda_{N'} \lambda'_{\gamma} \lambda_N} \tag{2.31}$$

where the N_{α} are normalization constants. The vector Π_{α} differs from $\tilde{\Pi}_{\alpha}$ in that the normalization is different from the case of the virtual photon spin density matrix. Apart from this distinction, they are the same. The summation takes place over the possible helicities of the virtual photon, λ_{γ}, and the target ,λ_N.

2.4 Angular Distributions

The angular distributions are examined in the rest frame of the ρ^0 meson. As described above, it is the direction of the positive pion in $\rho^0 \rightarrow \pi^+\pi^-$ that is used to describe the distributions. The normalized angular distributions, $W(\cos\theta, \phi)$, are given by [3]

$$\frac{dN}{d\cos\theta d\phi} \equiv W(\cos\theta, \phi) = \frac{3}{4\pi} \sum_{\lambda_V \lambda'_V} D^{1}_{\lambda_V 0}(\phi, \theta, -\phi)^{*} \rho(V)_{\lambda_V \lambda'_V} D^{1}_{\lambda'_V 0}(\phi, \theta, -\phi) \tag{2.32}$$

where the $D^{1}_{\lambda_V 0}$ are the Wigner rotation functions. Using the decomposition of the ρ^0 spin density matrix, Eqn. (2.30), the angular distributions can be written in terms of the ρ^{α}_{ik} and will also become dependent on the angle Φ. Measuring the angular distribution, $W(\cos\theta, \phi, \Phi)$, is therefore equivalent to determining the matrix elements, ρ^{α}_{ik} and, in turn, the helicity amplitudes $T_{\lambda_V \lambda_N \lambda_{\gamma} \lambda'_N}$.

It would appear that there are many matrix elements to be determined. Fortunately, the Σ^α matrices and the helicity amplitudes have symmetry properties which reduces the number of independent real quantities in the ρ^α_{ik} to 26. In the case of an unpolarized positron beam, 18 of the matrix elements ρ^α_{ik} can be determined as well as the ratio $R{=}\sigma_L/\sigma_T$, the ratio of cross sections for elastic ρ^0 production from longitudinally and transversely polarized photons. The angular distribution in this case is given by

$$
\begin{aligned}
W^{unpol}(\cos\theta,\phi,\Phi) = {} & \frac{1}{1+\epsilon R}\frac{3}{4\pi}\times \\
& \Big[\tfrac{1}{2}(1-\rho^0_{00}) + \tfrac{1}{2}(3\rho^0_{00}-1)\cos^2\theta - \sqrt{2}\,\mathrm{Re}\,\rho^0_{10}\sin 2\theta\cos\phi - \rho^0_{1-1}\sin^2\theta\cos 2\phi \\
& - \epsilon\cos 2\Phi\{\rho^1_{11}\sin^2\theta + \rho^1_{00}\cos^2\theta - \sqrt{2}\,\mathrm{Re}\,\rho^1_{10}\sin 2\theta\cos\phi - \rho^1_{1-1}\sin^2\theta\cos 2\phi\} \\
& \quad - \epsilon\sin 2\Phi\{\sqrt{2}\,\mathrm{Im}\,\rho^2_{10}\sin 2\theta\sin\phi + \mathrm{Im}\,\rho^2_{1-1}\sin^2\theta\sin 2\phi\} \\
& \quad + \epsilon R\{\tfrac{1}{2}(1-\rho^4_{00}) + \tfrac{1}{2}(3\rho^4_{00}-1)\cos^2\theta - \sqrt{2}\,\mathrm{Re}\,\rho^4_{10}\sin 2\theta\cos\phi \\
& \qquad - \rho^4_{1-1}\sin^2\theta\cos 2\phi\} \\
& \quad + \sqrt{2\epsilon R(1+\epsilon)}\cos\Phi\{\rho^5_{11}\sin^2\theta + \rho^5_{00}\cos^2\theta - \sqrt{2}\,\mathrm{Re}\,\rho^5_{10}\sin 2\theta\cos\phi \\
& \qquad - \rho^5_{1-1}\sin^2\theta\cos 2\phi\} \\
& \quad + \sqrt{2\epsilon R(1+\epsilon)}\sin\Phi\{\sqrt{2}\,\mathrm{Im}\,\rho^6_{10}\sin 2\theta\sin\phi + \mathrm{Im}\,\rho^6_{1-1}\sin^2\theta\sin 2\phi\}\Big].
\end{aligned}
\tag{2.33}
$$

For the case of longitudinally polarized positrons, a further 8 matrix elements can be determined. The expression for the angular distribution in the unpolarized situation will have the following expression added (subtracted) if the spins of the positrons are parallel (anti-parallel) to their momentum

$$W^{longpol}(\cos\theta,\phi,\Phi) = \frac{1}{1+\epsilon R}\frac{3}{4\pi}\times$$

$$
\begin{aligned}
P\Big[&\sqrt{1-\epsilon^2}\{\sqrt{2}\,\mathrm{Im}\,\rho^3_{10}\sin 2\theta\sin\phi + \mathrm{Im}\,\rho^3_{1-1}\sin^2\theta\sin 2\phi\}\\
&+\sqrt{2\epsilon(1-\epsilon)R}\cos\Phi\{\sqrt{2}\,\mathrm{Im}\,\rho^7_{10}\sin 2\theta\sin\phi\\
&\qquad\qquad + \mathrm{Im}\,\rho^7_{1-1}\sin^2\theta\sin 2\phi\}\\
&+\sqrt{2\epsilon(1-\epsilon)R}\sin\Phi\{\rho^8_{11}\sin^2\theta + \rho^8_{00}\cos^2\theta\\
&\qquad - \sqrt{2}\,\mathrm{Re}\,\rho^8_{10}\sin 2\theta\cos\phi - \sqrt{2}\rho^8_{1-1}\sin^2\theta\cos 2\phi\}\Big].
\end{aligned}
\tag{2.34}
$$

It is difficult to isolate the separate contributions from longitudinally and transversely polarized photons. To do this requires that measurements be taken at different lepton scattering angles, θ_{lab}, which can be difficult because the cross section falls off rapidly as the angle increases. In this case, the longitudinal and transverse contributions are combined in the following redefinition

$$r^{04}_{ik} = \frac{\rho^0_{ik} + \epsilon R\rho^4_{ik}}{1+\epsilon R} \tag{2.35}$$

$$r^{\alpha}_{ik} = \frac{\rho^{\alpha}_{ik}}{1+\epsilon R} \quad (\alpha = 1-3) \tag{2.36}$$

$$r^{\alpha}_{ik} = \frac{\sqrt{R}\rho^{\alpha}_{ik}}{1+\epsilon R} \quad (\alpha = 5-8). \tag{2.37}$$

The expressions for the angular distribution are then written as

$$
\begin{aligned}
W^{unpol}(\cos\theta,\phi,\Phi) = \frac{3}{4\pi}\times&\\
\Big[\tfrac{1}{2}(1-r^{04}_{00}) + \tfrac{1}{2}(3r^{04}_{00}-1)\cos^2\theta - \sqrt{2}\,\mathrm{Re}\,r^{04}_{10}\sin 2\theta\cos\phi - r^{04}_{1-1}\sin^2\theta\cos 2\phi&\\
-\epsilon\cos 2\Phi\{r^1_{11}\sin^2\theta + r^1_{00}\cos^2\theta - \sqrt{2}\,\mathrm{Re}\,r^1_{10}\sin 2\theta\cos\phi - r^1_{1-1}\sin^2\theta\cos 2\phi\}&\\
-\epsilon\sin 2\Phi\{\sqrt{2}\,\mathrm{Im}\,r^2_{10}\sin 2\theta\sin\phi + \mathrm{Im}\,r^2_{1-1}\sin^2\theta\sin 2\phi\}&\\
+\sqrt{2\epsilon(1+\epsilon)}\cos\Phi\{r^5_{11}\sin^2\theta + r^5_{00}\cos^2\theta - \sqrt{2}\,\mathrm{Re}\,r^5_{10}\sin 2\theta\cos\phi&\\
- r^5_{1-1}\sin^2\theta\cos 2\phi\}&
\end{aligned}
$$

$$+\sqrt{2\epsilon(1+\epsilon)}\sin\Phi\{\sqrt{2}\,\mathrm{Im}\,r^6_{10}\sin 2\theta\sin\phi+\mathrm{Im}\,r^6_{1-1}\sin^2\theta\sin 2\phi\}\Big] \tag{2.38}$$

and

$$\begin{aligned} W^{longpol}(\cos\theta,\phi,\Phi) = {} & \frac{3}{4\pi}\times \\ & P\Big[\sqrt{1-\epsilon^2}\{\sqrt{2}\,\mathrm{Im}\,r^3_{10}\sin 2\theta\sin\phi+\mathrm{Im}\,r^3_{1-1}\sin^2\theta\sin 2\phi\} \\ & +\sqrt{2\epsilon(1-\epsilon)}\cos\Phi\{\sqrt{2}\,\mathrm{Im}\,r^7_{10}\sin 2\theta\sin\phi+\mathrm{Im}\,r^7_{1-1}\sin^2\theta\sin 2\phi\} \\ & +\sqrt{2\epsilon(1-\epsilon)}\sin\Phi\{r^8_{11}\sin^2\theta+r^8_{00}\cos^2\theta \\ & -\sqrt{2}\,\mathrm{Re}\,r^8_{10}\sin 2\theta\cos\phi-\sqrt{2}\,\mathrm{Re}\,r^8_{1-1}\sin^2\theta\cos 2\phi\}\Big] \end{aligned} \tag{2.39}$$

The number of matrix elements to be determined is still quite large. If there is helicity conservation in the s-channel as will be discussed in the next section, then the number of independent matrix elements is reduced even further. This model will be assumed in the analysis.

2.5 s-Channel Helicity Conservation

It is of experimental interest to examine whether or not the ρ^0 carries the same helicity as the virtual photon as expected by the VDM. This model is called s-channel helicity conservation (SCHC). It will also be assumed that the parity of the particles (or system of particles) with angular momentum l exchanged between the target and γ^*-ρ^0 system has natural parity, P= $(-1)^l$. Assuming SCHC, a number of helicity amplitudes that allow for longitudinally (transversely) polarized ρ^0 mesons to be produced from transversely (longitudinally) polarized photons are set to zero. In this case, there remains only two independent helicity amplitudes, ($T_{0\frac{1}{2}0\frac{1}{2}}$ and $T_{1\frac{1}{2}1\frac{1}{2}}$). The expressions given in Eqns.(2.38) and (2.39) become

$$
\begin{aligned}
W(\cos\theta,\phi,\Phi) = \frac{3}{4\pi}\Big[&\frac{1}{2}\{(1-\cos^2\theta + r^{04}_{00}(3\cos^2\theta - 1)\} \\
&+ r^1_{1-1}\epsilon\cos 2\Phi\sin^2\theta\cos 2\phi \\
&- \mathrm{Im}\, r^2_{1-1}\epsilon\sin 2\Phi\sin^2\theta\sin 2\phi \\
&- 2\sqrt{\epsilon(1+\epsilon)}\mathrm{Re}\, r^5_{10}\cos\Phi\sin 2\theta\cos\phi \\
&+ 2\sqrt{\epsilon(1+\epsilon)}\mathrm{Im}\, r^6_{10}\sin\Phi\sin 2\theta\sin\phi \\
&+ 2P\sqrt{\epsilon(1-\epsilon)}\{\mathrm{Im}\, r^7_{10}\cos\Phi\sin 2\theta\sin\phi \\
&- \mathrm{Re}\, r^8_{10}\sin\Phi\sin 2\theta\cos\phi\}\Big]
\end{aligned}
\tag{2.40}
$$

where incident positrons with a positive helicity are assumed.

The value of r^{04}_{00} is related to the probability that longitudinally polarized ρ^0s are produced and is determined by the distribution in $\cos\theta$. This by itself does not distinguish between longitudinally polarized ρ^0 mesons originating from longitudinally or transversely polarized photons. However, for transversely polarized ρ^0s, the contribution from transversely polarized photons can be identified by obtaining a non-zero value for r^1_{1-1}. SCHC predicts that r^{04}_{00} is related to r^1_{1-1} by the equation

$$
r^1_{1-1} = \frac{1}{2}(1 - r^{04}_{00}). \tag{2.41}
$$

The elements ρ^5_{10} and ρ^6_{10} are not independent as well and can be specified by one parameter, δ, the relative phase angle between the two remaining helicity amplitudes

$$
T_{0\frac{1}{2}0\frac{1}{2}}T^*_{1\frac{1}{2}1\frac{1}{2}} = |T_{0\frac{1}{2}0\frac{1}{2}}||T_{1\frac{1}{2}1\frac{1}{2}}|e^{-i\delta}, \tag{2.42}
$$

and the following relationships hold true

$$\mathrm{Re}\, r^5_{10} = -\mathrm{Im}\, r^6_{10} \quad \mathrm{Im}\, r^5_{10} = \mathrm{Re}\, r^6_{10}. \tag{2.43}$$

Other relationships between matrix elements can be made with the assumption of SCHC: $r^1_{1-1} = -\mathrm{Im}\, r^2_{1-1}$, $r^5_{10} = r^7_{10}$, and $r^6_{10} = r^8_{10}$.

The angles ϕ and Φ are also no longer independent when assuming SCHC and natural parity exchange. With the definition, $\psi = \phi - \Phi$, the expression for the angular distribution can be given as

$$\begin{aligned} W(\cos\theta, \psi) = \frac{1}{1+\epsilon R}\frac{3}{8\pi}\Big[& \sin^2\theta(1+\epsilon\cos 2\psi) + 2\epsilon R\cos^2\theta \\ & - \sqrt{2\epsilon(1+\epsilon)R}\cos\delta\sin 2\theta\cos\psi \\ & + P\sqrt{2\epsilon(1-\epsilon)R}\sin\delta\sin 2\theta\sin\psi\Big]. \end{aligned} \tag{2.44}$$

2.6 Other Considerations

Because the production target in this study was ^{3}He, there are some concerns that may affect the treatment of the data.

2.6.1 Coherent vs. Incoherent Scattering

There is an additional issue when considering elastic production of vector mesons on a nuclear target consisting of more than one nucleon. The scattering can effectively take place from the entire nucleus or from one of its constituent nucleons; this is called coherent and incoherent scattering, respectively.

There are differences in the kinematics and cross section in each of these cases. The kinematics are affected because the effective mass of the target is different. The cross section depends on the size of the target according to Eqn.(2.13). It is not clear whether there is an effect on the physics of the helicity transfer between the incoming γ^* and outgoing ρ^0.

2.6.2 Diffractive Dissociation

In a fraction of events, the momentum transfer to a target nucleon will allow it to fragment; this is called diffractive dissociation (Figure 2.5). This contribution in the HERMES 1995 data cannot be separated out and the size of this effect is undetermined. For the case where the target remains intact, $\Delta E \approx 0$, but in the case of an event where diffractive dissociation takes place, $M_X > M_{targ}$ and gives $\Delta E > 0$. The shape of the contribution expected in the HERMES experiment is shown in Figure 2.6.

It will be assumed for this study that the dissociation at the nucleon vertex has no effect on the physics at the γ^*-ρ^0 vertex.

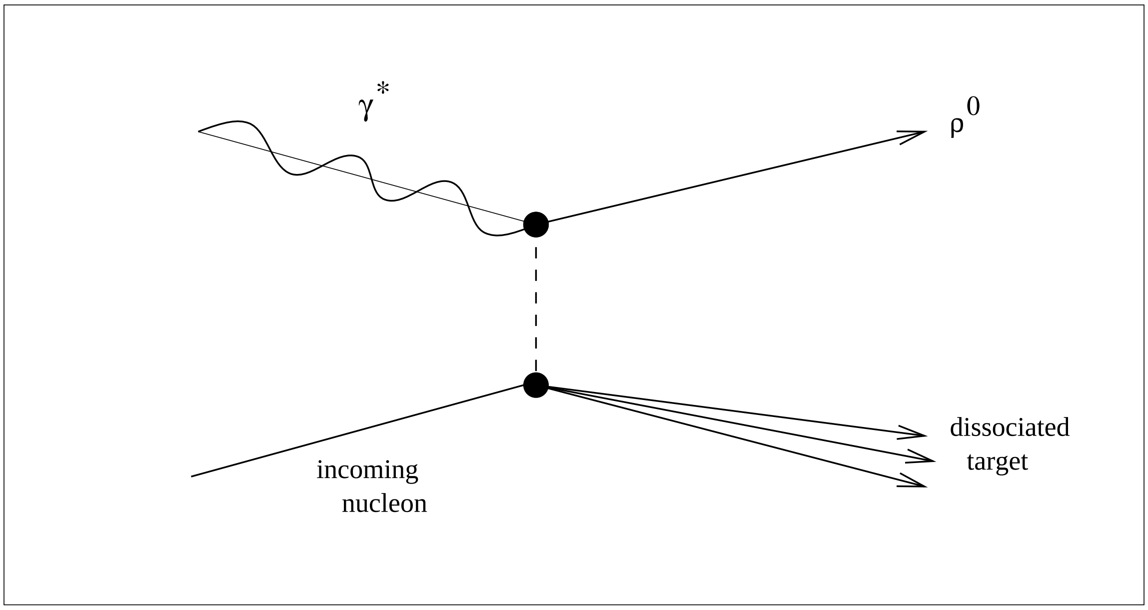

Figure 2.5: Illustration of diffractive dissociation.

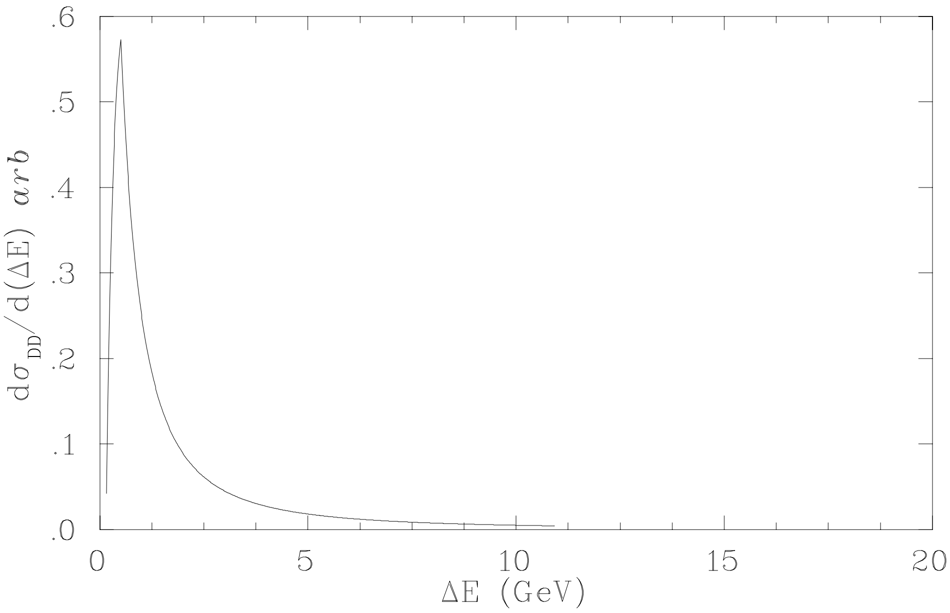

Figure 2.6: Expected distribution in ΔE of the contribution due to diffractive dissociation.

CHAPTER 3

HERA and the HERMES Spectrometer

HERMES is a fixed target experiment and was designed to track and identify scattered particles in inclusive and semi-inclusive measurements from DIS processes. In 1995, positrons with an energy of 27.5 GeV were incident on a ^{3}He internal gas target to yield reactions of the form $^3\mathrm{He}(e^+, e^+X)$. While inclusive and semi-inclusive measurements were in mind when the spectrometer was designed, the study of elastically produced ρ^0 mesons requires that all three particles in the final state (not including the recoiling target) be detected, an exclusive measurement. This chapter will provide a description of the polarized positron beam and ^{3}He target in addition to a discussion on the components of the spectrometer.

3.1 The HERA Positron Beam

The HERMES experiment is located in the HERA East Hall of DESY (Deutsches Elektronen-Synchrotron) in Hamburg, Germany. The HERA storage ring is 6.3 km in circumference with positrons and protons circulating in opposite directions with energies of 27.5 and 820 GeV, respectively. HERMES uses the positron beam only. The positrons and protons travel in separate beamlines except in the interaction regions of the two collider experiments, H1 and ZEUS, also located at HERA in the North and South Halls. All three experiments simultaneously make use of the positron beam.

The positron 'beam' is not continuous, but consists of 180 bunches with each having dimensions of 8.3 mm(length) $\times$ 280 μm(horizontal) $\times$ 50 μm(vertical). At the start of a fill, the bunches are injected into and evenly distributed about the ring at an energy of 12 GeV and then brought up to the full energy of 27.5 GeV. The maximum currents are obtained at the beginning of a fill and are around 58 mA. Various factors contribute to losses in the beam current including scattering from the ^{3}He target and in the H1 and ZEUS interaction regions. The result is an exponential decay in the current with a lifetime on the order of 10 hr. When the current reaches a value of $\sim$11 mA, the beam is dumped and a new fill is started.

Strong magnetic fields are required to keep charged particles travelling in a curved path and circulating in the storage ring. For the positron beam, this is a field with a peak value of 0.274 T. The field is transverse to the particle motion and allows for a natural build-up of transverse polarization in the positron beam; this is called the Sokolov–Ternov effect and is used to obtain the necessary polarization for the HERMES experiment. Spin rotators, discussed below, convert the polarization of the beam from transverse to longitudinal. A schematic diagram of HERA and the polarized beam is shown in Figure 3.1.

The basis of the Sokolov–Ternov effect is that there is a slightly greater probability of aligning the positron spin parallel to the field when the positron emits synchrotron radiation. The rates of a spin-flip parallel and anti-parallel to a homogeneous magnetic field, respectively, are given by:

$$\omega^{\uparrow\uparrow} = \frac{1}{2\tau_P}(1 + \frac{8\sqrt{3}}{15}) \tag{3.1}$$

$$\omega^{\uparrow\downarrow} = \frac{1}{2\tau_P}(1 - \frac{8\sqrt{3}}{15}) \tag{3.2}$$

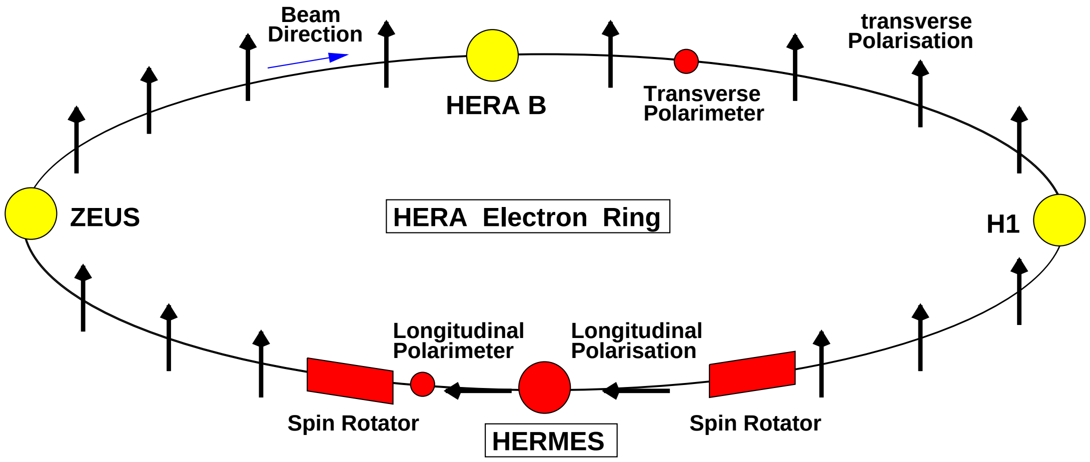

Figure 3.1: Schematic of the HERA positron storage ring. The polarization is changed from transverse to longitudinal and back as the beam travels through the spin rotators.

where

$$\tau_P = \frac{R^3}{\gamma^5} \cdot (2.83{\times}10^{18} \ \ \mathrm{s/m^3}). \tag{3.3}$$

The radius of the positron trajectory in the magnetic field is given by R and γ is the usual relativistic parameter. The average radius of the HERA storage ring is 707 m yielding the rates $\omega^{\uparrow\uparrow} = 1.56\ \mathrm{h}^{-1}$ and $\omega^{\uparrow\downarrow} = 0.062\ \mathrm{h}^{-1}$. Defining $N^{\uparrow\uparrow}$ and $N^{\uparrow\downarrow}$ to be the number of positrons in the storage ring with spins parallel and anti-parallel to the field, respectively, the polarization of the beam is given by

$$P = \frac{N^{\uparrow\uparrow} - N^{\uparrow\downarrow}}{N^{\uparrow\uparrow} + N^{\uparrow\downarrow}}. \tag{3.4}$$

The build-up of polarization in the beam as a function of time is

$$P(t) = P_{max}(1 - e^{-t/\tau_P}). \tag{3.5}$$

The value of $P_{max} = 92.38\%$ is the largest attainable polarization. In practice, the value of P_{max} is difficult to obtain due to various depolarizing effects such as the presence of misaligned quadrupole magnets.

The natural transverse polarization of the positrons is not suitable for the HERMES physics program which dictates the use of a longitudinally polarized beam. Longitudinal polarization is also desirable in the study of elastically produced ρ^0 mesons as the effects due to transverse polarization are negligible unless $Q^2 \approx m^2$. Spin rotators have therefore been installed along the beamline before and after the experimental area. They consist of a set of horizontally and vertically positioned dipole magnets and have the effect of rotating the spin of the positrons in the storage ring by 90° so they travel through the HERMES target region longitudinally polarized. The spin rotators located after the experiment are to bring the positrons back to the original transverse polarization state.

A polarimeter in the HERA West Hall is used to measure the transverse polarization of the positron beam. Circularly polarized photons from an argon laser are backscattered from the beam and detected. The spin dependence of the scattering cross section is used to determine the polarization of the positrons.

3.2 Target

The target in 1995 consisted of a pure ^{3}He gas. The gas was pumped to a storage cell through which the HERA positron beam travelled. The dimensions of the cell were 9.8 mm × 29.0 mm × 400 mm. Gas pumped inside the cell was allowed to flow out the ends and removed via a high performance pumping system to maintain an optimum gas density while minimizing the effect on beam lifetime. A

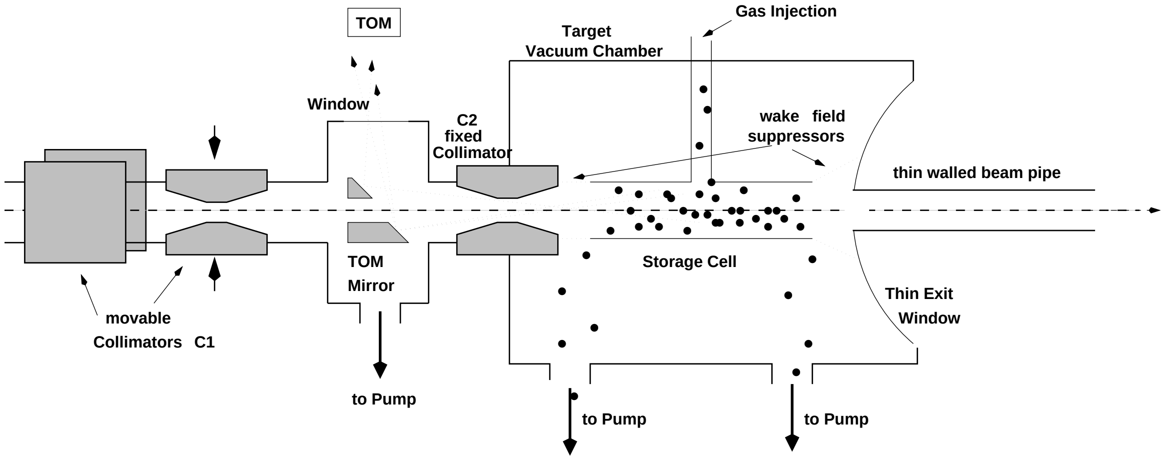

Figure 3.2: Schematic diagram of the HERMES ^{3}He target.

schematic diagram of the target is shown in Figure 3.2 and the gas density profile is shown in Figure 3.3. Final state particles leaving the target and travelling into the spectrometer acceptance pass through a 0.3 mm thin stainless steel foil. The target is protected from synchrotron radiation generated upstream of the target by a system of movable collimators. The source was changed for 1996-1997 to accomodate running with polarized hydrogen and deuterium.

The ^{3}He source delivered atoms polarized in a pumping cell to the target cell through a feed tube. In the pumping cell, a weak electrical discharge excited some ^{3}He atoms to a 2^3S_1 metastable state which then were polarized by circularly polarized laser light in a transition to the 2^3P_0 state. The direction of the polarization was defined by a 10 G homogeneous magnetic field. Ground state atoms were then polarized by the 2^3P_0 atoms in metastability exchange collisions. The degree of polarization that could be obtained was around 50-60% with the spin orientation being flipped every 10 minutes by changing the polarizing laser light. The polarization of the gas was measured in both the pumping and target cells and agreed well. A detailed description of the target can be found in [5].

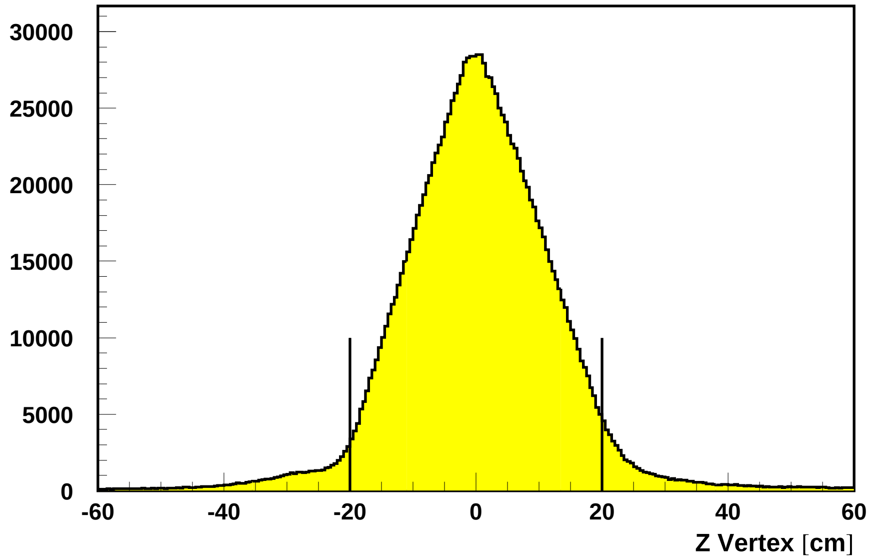

Figure 3.3: The longitudinal gas density profile in the HERMES ^{3}He target cell determined from the origin of reconstructed tracks. The spatial extent of the target cell is indicated by the lines.

3.3 Spectrometer

The purpose of the HERMES spectrometer is to determine the momentum of particles resulting from interactions in the target. Charged particles travelling through a magnetic field are deflected and are detected as they pass through tracking chambers. A large magnet in conjunction with tracking chambers in the front and back regions were used to determine the momentum of charged particles. (The front region is the target side of the magnet.) There were also four components used for particle identification (PID): a transition radiation detector, a threshold Cerenkov, an electromagnetic calorimeter and a preshower counter. A cut-away view of the detector is given in Figure 3.4 and a more schematic side view is shown in Figure 3.5.

The origin of the coordinate system used for the spectrometer is at the center of the target. The positive z-axis is along the direction of the positron beam. The

y-axis is oriented vertically and the x-axis is the remaining direction in a right-handed coordinate system: into the plane of the page when looking at Figure 3.5.

While HERMES is a fixed target scattering experiment and uses only a positron beam, the HERA machine also has protons circulating in the opposite direction and in a separate beam line. The proton beam travels antiparallel to the positron beam through the spectrometer separated by a distance of 72 cm. This meant that the spectrometer had to be separated into an upper and lower half. The resulting acceptance of the spectrometer is

$$40 \ \text{mrad} < |\theta_{vert}| < 140 \ \text{mrad}, \quad |\theta_{horiz}| < 170 \ \text{mrad} \tag{3.6}$$

where θ_{vert} and θ_{horiz} are the vertical and horizontal angles with respect to the beam axis as seen from the target.

The magnetic field is provided by a large H-frame water-cooled dipole magnet. The deflecting power is $\int Bdl = 1.3$ Tm and consumes 300 kW of power. Field clamps are positioned on either side of the magnet to minimize the stray field in the vicinity of the tracking chambers. A shielding plate is also used to protect the beams as much as possible from the field of the magnet.

The following is a brief description of the components of the HERMES spectrometer as it was in 1995. A full description can be found in the Technical Design Report [6] and [7].

3.3.1 Tracking Chambers

The purpose of the tracking chambers is to determine the path of the scattered positrons and charged particles produced in the interaction. Because the particles are

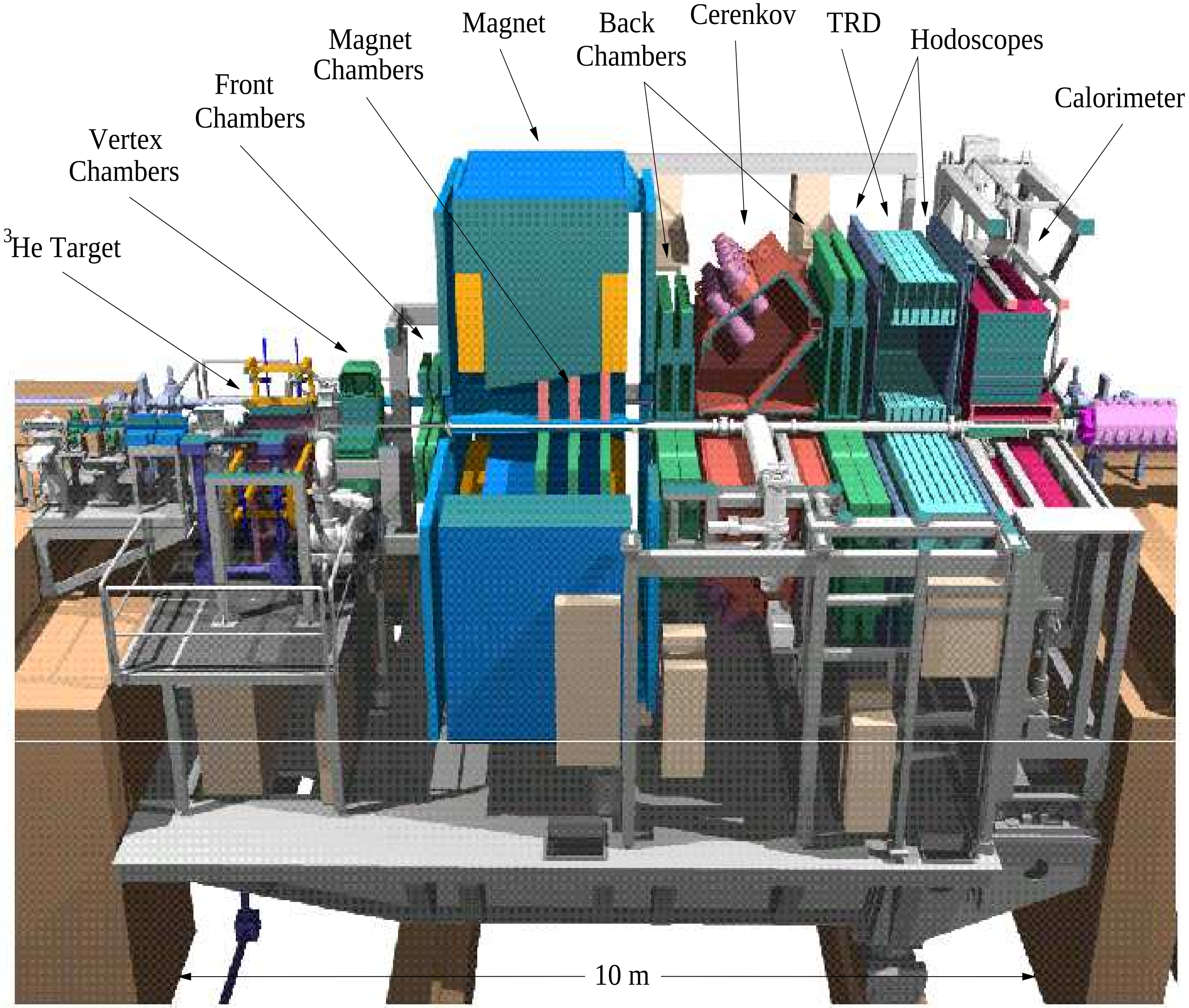

Figure 3.4: Schematic cut-away view of the HERMES spectrometer.

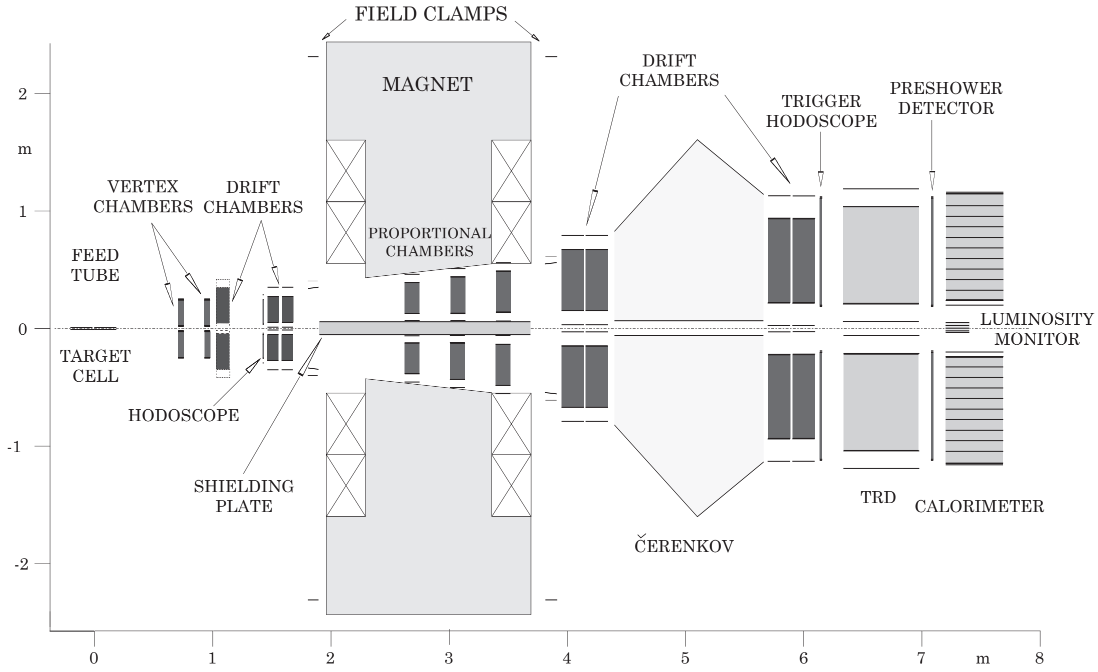

Figure 3.5: Schematic side view of the HERMES spectrometer. The hodoscope shown between the front and vertex chambers was not present in 1995.

deflected in the magnetic field, the momentum of the particles can be found. Outside of the magnet, the particle paths are basically straight lines. Also, the origin of particle paths can be found. As tracks of interest will generally originate in the target, tracks not meeting this condition can be rejected.

Charged particles passing through a tracking chamber ionize a gas and the resulting charge then drifts in an electric field toward an anodic sensing wire. The collected charge provides a signal that can be detected. The time for the charge to be produced to the time it is collected can be measured and the difference is used to find the distance from the anode wire to where the particle passed through the detector. This is a simple explanation of the operation of a tracking chamber; more details can be found in [8].

The tracking chambers are arranged as follows: the vertex chambers (VC 1/2) are located just outside the target window. These, along with the front chambers (FC 1/2) constitute the tracking capabilites in the front of the magnet. The back chambers (BC 1/2/3/4) are for tracking particles after the magnet. The magnet chambers (MC 1/2/3) are located inside of the magnet itself. See Figure 3.4. The front and back chambers are conventional drift chambers. They each consist of two modules with each module containing three planes. The planes are oriented in three different directions (0° (vertical), $\pm 30^\circ$) so that a space point can be calculated in three different ways.

The vertex chambers are of different construction than the front and back chambers: they are microstrip gas chambers. The arrangement of planes in the detector is the same. However, instead of wires aluminum strips on a thin glass substrate are used. In 1995, problems with the vertex chambers made it unfeasible for them to be used in track reconstruction.

The magnet chambers are located inside of the magnet. They are standard proportional chambers and are used to help in matching tracks in the front region to tracks in the back region which can be difficult for events with a high track multiplicity. Problems with the magnet chambers in 1995 did not allow them to be used for the reconstruction of events, but the track multiplicities were small enough that this did not present a serious difficulty.

Ideally, the tracks in the front region are matched to tracks in the back region through the magnet. However, with the unavailability of the vertex and magnet chambers, only the front chambers were able to provide tracking in the front region. A strategy was developed where tracks from the back region were projected to a point in the middle of the magnet. Corresponding tracks in the front region were made to coincide with this point to give improved resolution in the front region. The reconstruction of events is performed by the HERMES reconstruction program, HRC [9]. An example of a reconstructed event is shown in Figure 3.6.

3.3.2 Particle Identification Detectors

One major issue that concerns most of the analyses of HERMES physics is the identification of the scattered positron and other particles (pions, kaons, protons, etc.) Four PID detectors are used in the experiment. Responses from the detectors are able to be associated with the track of a particle after track reconstruction has been performed thereby yielding PID and momentum information for each detected particle.

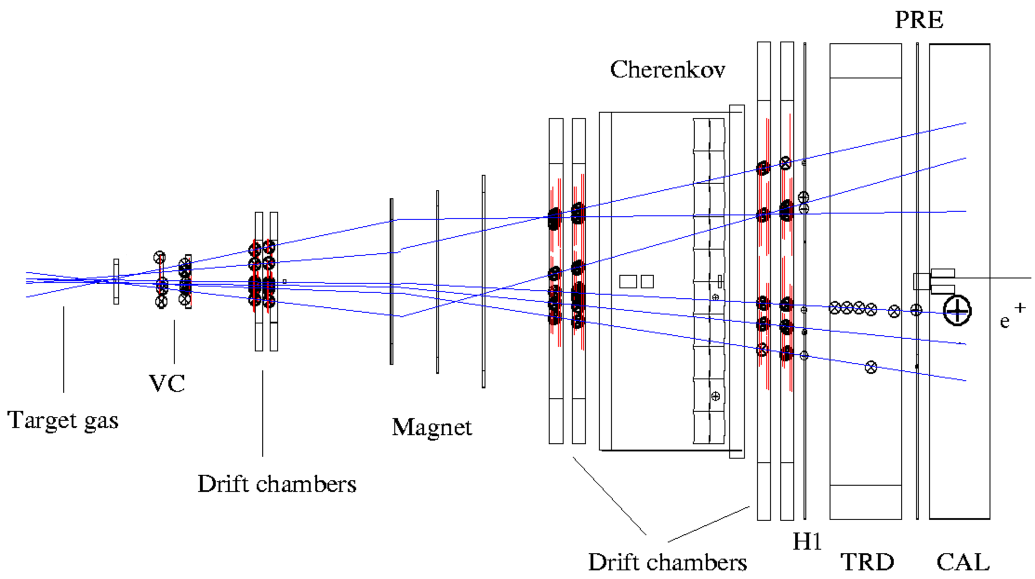

Figure 3.6: Example of a reconstructed DIS event.

Transition Radiation Detector

A transition radiation detector (TRD) is based on the principle that a charged particle has a finite probability that it will emit photons (transition radiation or TR) when it passes through an interface of materials with different dielectric constants [10]. The number of TR photons emitted per interface is approximately $\frac{2}{3}\alpha$ where $\alpha = \frac{1}{137}$ is the fine structure constant. For the case of relativistic particles, the total energy emitted is proportional to $\gamma = E/mc^2$. The yield of TR photons is enhanced by employing a large number of dielectric interfaces. This provides a good method of particle identification when discrimination between positrons(electrons) and hadrons is desired.

The radiator of each TRD module consists of a 6.35 cm thick matrix of 17-20 μm propylene fibers that are randomly oriented in two dimensions and effectively

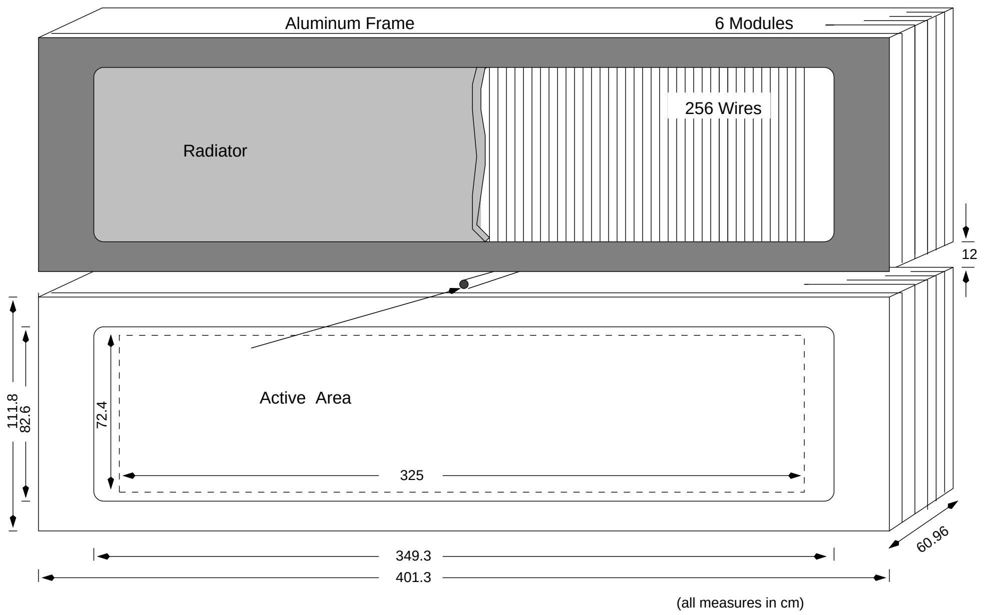

Figure 3.7: Schematic view of the TRD. There are six modules in each of the top and bottom halves of the spectrometer.

provides about 270 layers that the incident particle must cross. The energy of the TR photons is in the range 2-15 keV corresponding to the X-ray part of the electromagnetic spectrum. The X-rays are subsequently detected in a proportional chamber with 256 wires. A schematic diagram of the TRD is shown in Figure 3.7. The chamber is filled with a Xe:CH_4(90:10) gas mixture for efficient X-ray absorption. Xenon is expensive and is continuously recirculated through the detector. To minimize the amount of oxygen and nitrogen contamination, CO_2 is circulated through flush gaps on either side of the chamber.

For the optimum positron-pion separation in the space available, six TRD modules are used in the experiment. Incident particles may produce energetic electrons which lead to a larger signal than otherwise would be expected. The response of the detector is therefore calculated using the truncated mean by throwing out the value for the largest signal of the six modules and taking the average of the remaining five. Also, TR radiation is emitted within a narrow cone of angle $1/\gamma$ in the direction of the particle's momentum, so the signal obtained is a contribution from both ionization in the gas and transition radiation. The response distributions for positrons and pions are shown in Figure 3.8. When the TRD functions at its optimal voltage, the pion rejection factor (PRF) exceeds the design goal of 100.

Threshold Cerenkov

Cerenkov radiation is emitted by particles with velocity v travelling faster than the speed of light permitted in a given medium. This speed is given by c/n where c is the speed of light in a vacuum and n is the index of refraction of the medium. The light is emitted in a cone with an axis along the particle's motion and a half-angle of $\arccos(1/nv)$. The measurement of this angle can be used to obtain a direct determination of the velocity of a particle. However, important information can be obtained by just observing if a particle emits Cerenkov light or not as in a threshold Cerenkov detector: particles of differing masses can be distinguished in a given range of momenta. HERMES employs such a threshold Cerenkov detector.

The threshold Cerenkov used in the experiment contains a 1 m path of N_2 gas at atmospheric pressure. The Cerenkov radiation is reflected by an array of mirrors to photo-multiplier tubes mounted on the detector. A diagram of the detector is shown in Figure 3.9.

For the HERMES Cerenkov detector, the momentum threshold for positrons and electrons to emit radiation is 0.021 GeV. More massive particles must have a higher momentum to radiate, for example, the momentum threshold for pions is 5.72 GeV. Thus, separation between positrons and pions is possible in this range of momenta. For even heavier particles, pion-kaon separation is possible for momenta

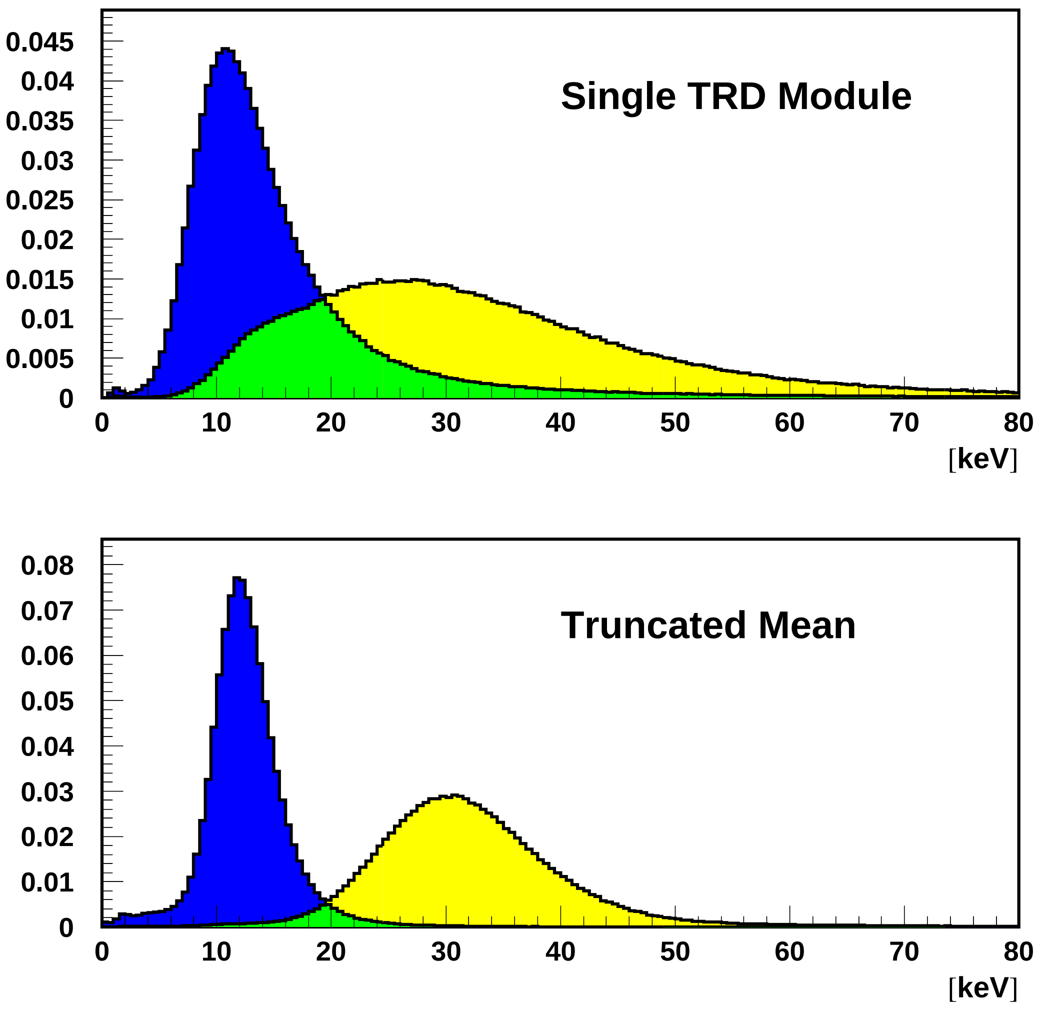

Figure 3.8: Response of the TRD to pions and positrons for a single module and entire detector using the method of the truncated mean. The distributions on the left and right correspond to pions and positrons, respectively.[11]

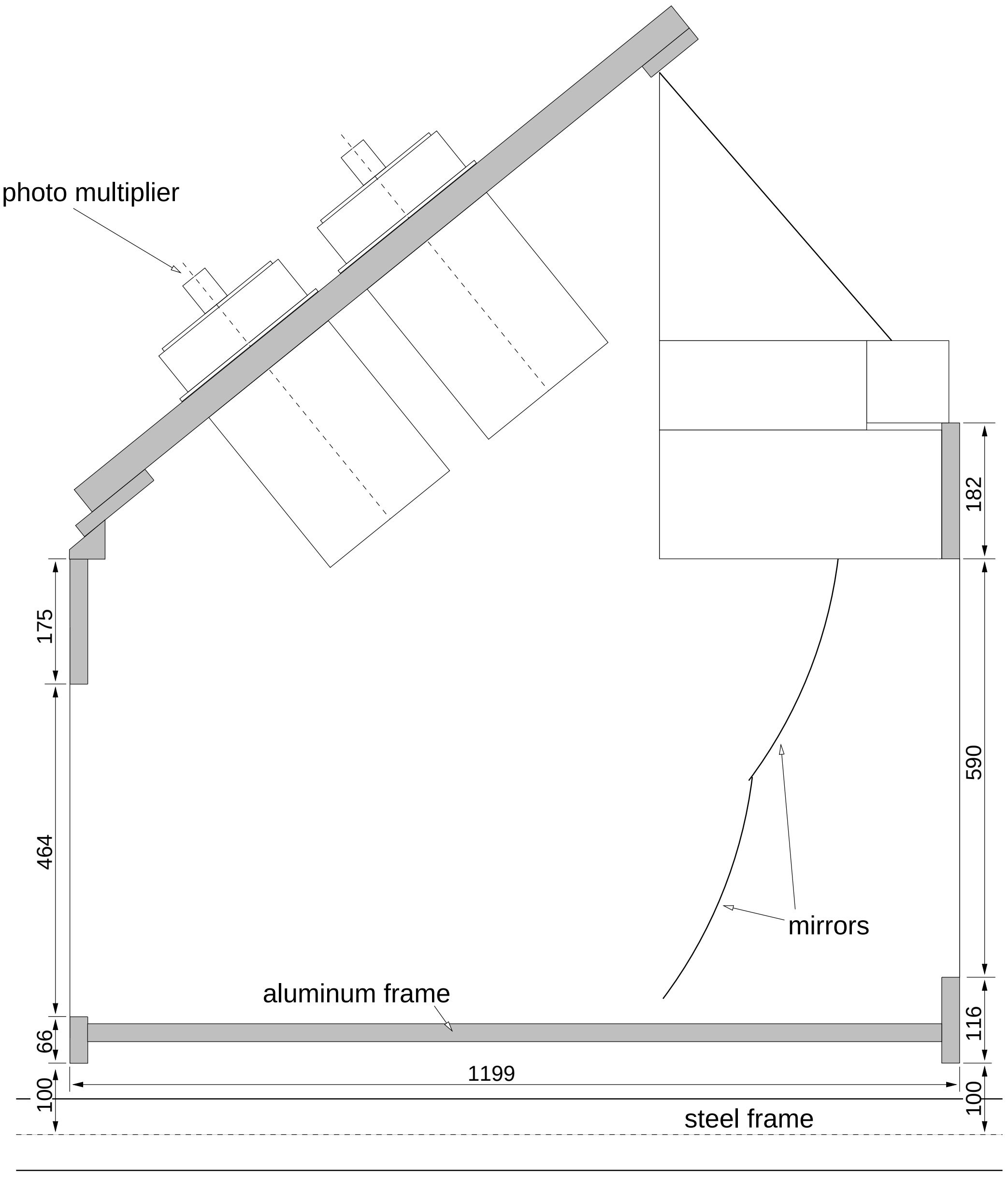

Figure 3.9: Schematic diagram of the Cerenkov detector (side view of upper half). Incident particles travel from left to right. A diagram of the lower half would appear as a mirror image reflected about a horizontal line at the bottom of the page.

of 5.72 GeV - 20.23 GeV and kaon-proton separation for momenta of 20.23 GeV - 38.42 GeV.

Electromagnetic Calorimeter

Electromagnetic showers develop when high energy positrons, electrons, and photons travel through material. Positrons and electons will lose their energy largely due to the emission of bremsstrahlung radiation and photons will convert into electron-positron pairs (pair production). The produced pairs and the bremsstrahlung photons are then able to undergo these same processes again and again to generate a shower until the energy has dissipated to the point where ionization losses become important. The energy at which losses from the generation of shower particles and ionization are equal is called the critical energy, E_C.

The purpose of the calorimeter is to contain the shower so that the energy of the incident positron or electron can be determined. The energy lost by a positron or electron is characterized by the radiation length of the material, X_0. It is defined as the average distance that an electron must travel and remains with all but $1/e$ of its original energy. The calorimeter was therefore designed to be several radiation lengths thick. Materials containing atoms of high atomic number typically have a smaller X_0.

The showers produced from hadrons (pions, for example) have different properties. The energy losses in this case are not due to bremsstrahlung, but rather due to ionization losses and inelastic hadronic interactions with the material of the calorimeter. A large variety of particles are created as a result of the hadronic interactions. The most important of these particles is the neutral pion which decays very quickly into two photons ($\pi^0 \to \gamma\gamma$). The photons can then undergo pair production and generate an electromagnetic cascade as described above. Whereas an electromagnetic shower starts as soon as the photon or electron enters the calorimeter, the shower due to a hadron will begin later and may not be entirely contained in the calorimeter.

The electromagnetic calorimeter at HERMES consists of two walls of F101 lead glass (one each for the top and bottom half of the spectrometer). The glass blocks of dimension 9 cm $\times$ 9 cm $\times$ 50 cm (18 radiation lengths) are arranged in rows of 42 $\times$ 10 to make each wall. Particles in the shower are still travelling at relativistic velocities and will emit Cerenkov radiation in the lead glass. Phototubes are therefore used to measure the energy deposition in each block. A diagram of the calorimeter is in Figure 3.10.

Electromagnetic showers are generally contained within a single block, but hadronic showers can have a large transverse dimension and may extend over adjacent blocks, so the measurements from a 3 $\times$ 3 block array are summed to give the total energy deposition of a given particle.

The calorimeter plays an important role in the first level trigger as well as in particle identification. The requirement of a local energy deposition in the calorimeter of at least 3.5 GeV provides a signal that a scattered positron may have been detected. In the offline analysis, the ratio of deposited energy to reconstructed momentum, E_{calo}/p, can be found and provides a means to distinguish between positrons and hadrons. Figure 3.11 shows the distributions of E_{calo}/p for positrons and hadrons.

Preshower

Immediately upstream and downstream of the TRD are two hodoscopes. Each hodscope is constructed of 42 plastic scintillator paddles with a phototube on the end of each paddle. A diagram of a single hodoscope is shown in Figure 3.12. The

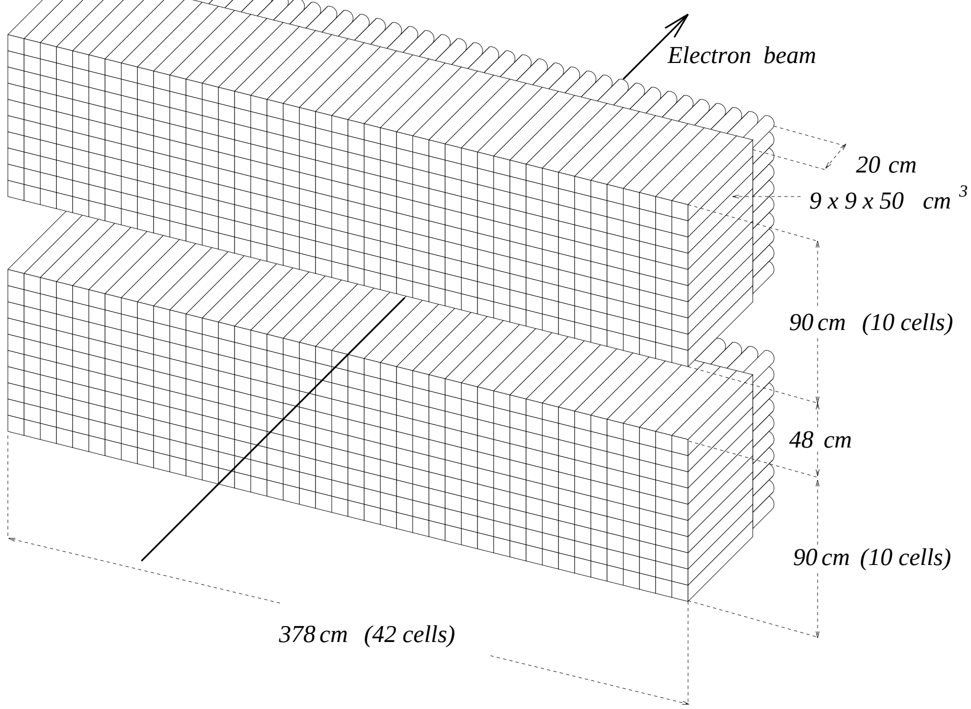

Figure 3.10: Schematic diagram of the electromagnetic calorimeter.

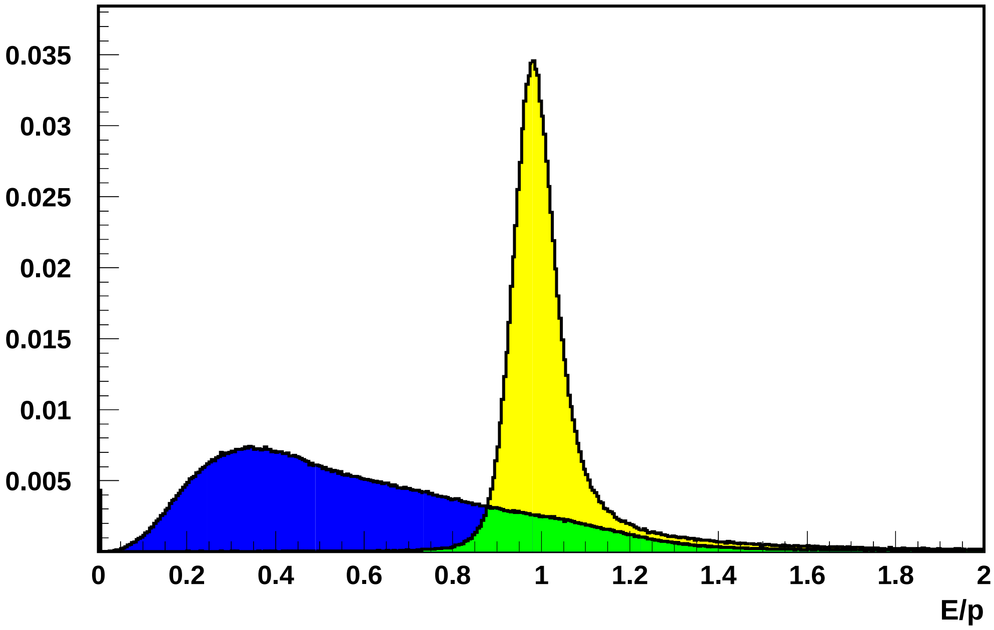

Figure 3.11: Response of the electomagnetic calorimeter. The positron peak is centered at $E/p = 1$ and the hadrons comprise the distribution for $E/p < 1$. [11]

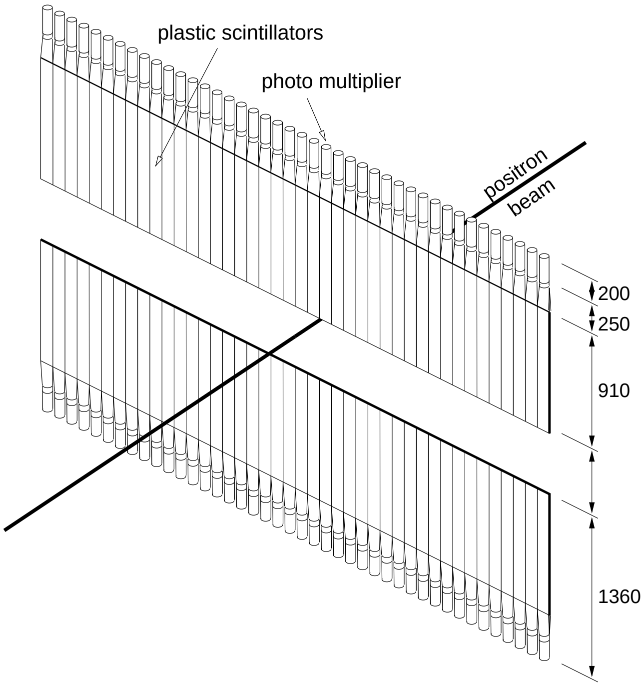

Figure 3.12: Schematic diagram of a hodoscope. A sheet of lead is placed in front of the second hodoscope to form the preshower detector.

second hodoscope has a 11 mm thick lead sheet immediately in front of it to form the preshower detector and provides additional particle identification capability.

The lead sheet is two radiation lengths thick. Positrons, electrons will begin a shower in the lead and the particles from the resulting shower are detected in the hodoscope. Hadrons, on the other hand, will not generally generate a shower but leave a smaller signal from ionization losses instead. The distributions of the preshower signal for positrons and hadrons are shown in Figure 3.13.

3.3.3 Luminosity Monitor

The luminosity is defined as the number of particles in a beam passing a given point per unit time per unit area. It is monitored by two 3×4 arrays of radiation

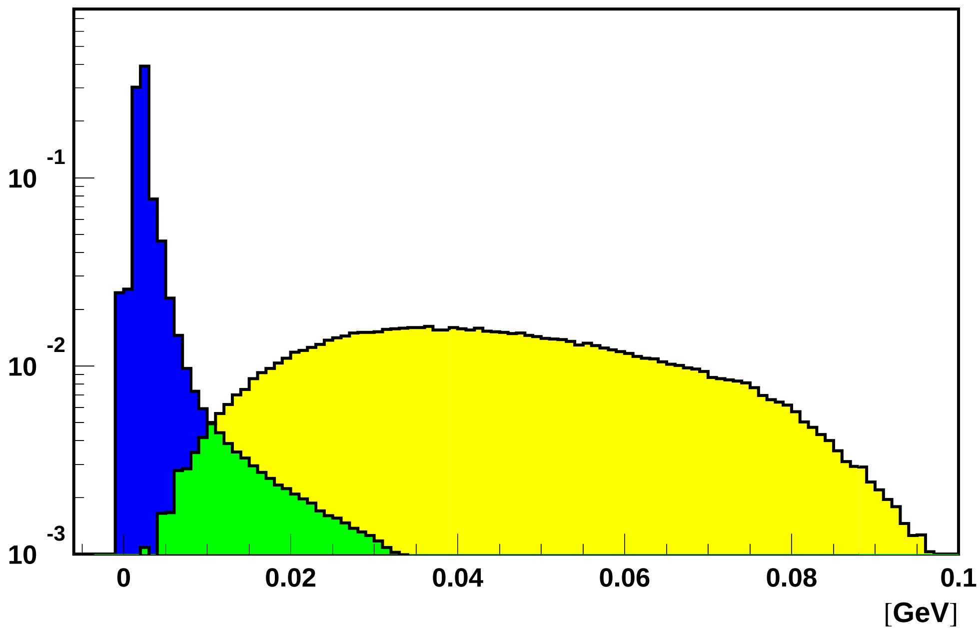

Figure 3.13: Response of the preshower detector. The peak corresponding to the hadron signal is on the left. The positrons leave a larger signal as seen on the right.[11]

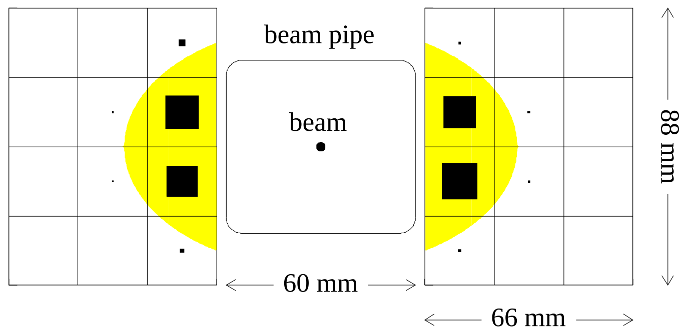

Figure 3.14: Schematic front view of the luminosity monitor. The size of the boxes represent the number of hits in each block. The shaded area shows the beam pipe acceptance.

hard $NaBi(WO_4)_2$ crystals located on opposite sides and close to the positron beam pipe at the position of the electromagnetic calorimeter. The blocks have dimensions 22 mm $\times$ 22 mm $\times$ 200 mm and a photomultiplier is placed on the back of each block. A diagram of the luminosity monitor is shown in Figure 3.14. The principle of operation is the same as for the electromagnetic calorimeter.

Positrons in the beam undergo Bhabha scattering ($e^+e^- \rightarrow e^+e^-$) and annihilation ($e^+e^- \rightarrow \gamma\gamma$) with the electrons of the target gas. The cross sections for these processes are very well known. The e^+e^- from Bhabha events can simultaneously deposit a large amount of energy in both the left and right side of the detector. For this to be possible, the beam pipe must widen from the target region to the position of the luminosity monitor and is shown in Figure 3.15. The rates at which coincidences from these Bhabha events occur provide a measurement of the luminosity.

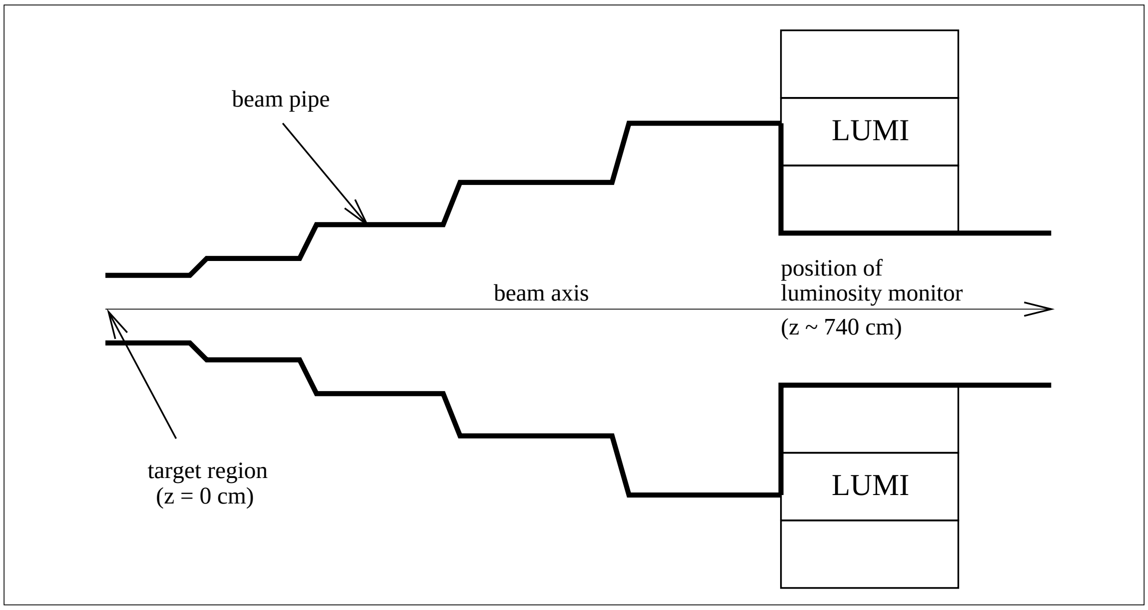

Figure 3.15: Schematic top view of the luminosity monitor and beam pipe. The beam pipe must widen to allow particles from the target region to be detected. This figure is not to scale.

3.3.4 Gain Monitoring System

The responses of the calorimeter, hodoscopes, and luminosity monitor have a time dependence which is monitored by the gain monitoring system (GMS). Pulses of laser light are sent through glass fibres to the photomultipliers of these detectors and to a reference photodiode. The signals from the PMTs are compared to the photodiode which has a stable response over time.

3.3.5 Trigger

The purpose of the trigger is to signal the readout electronics of the detectors when an event of interest occurs. In the case of the HERMES experiment, this is the detection of a positron from a deep inelastic scattering event. The first-level trigger was a coincidence of hits in the two hodoscopes, at least two hits in the back chambers, and a localized energy deposition in the calorimeter of a value greater than 3.5 GeV. The trigger was allowed if it came in a time window defined by the HERA clock which signaled the passing of a positron bunch.

For a positron beam current of 30 mA and a nominal ^{3}He gas density of 1.2×10^{15} nucleons/cm^2, the trigger rate for good events was 65 Hz. Background events are due to hadrons depositing usually large energy deposits in the calorimeter and showers from satellite bunches in the proton beam. The rate for background events was around 4 Hz.

CHAPTER 4

The Monte Carlo Programs

The HERMES Monte Carlo (HMC) [12, 13] is a computer simulation of the HERMES experiment. It can be thought as consisting of two separate components. The first component is the physics generator which provides a model of the positron-target interactions. The second component is the simulation of the final state particles from this interaction travelling through a model of the spectrometer.

The program was designed to simulate the measurement of g_1^n and g_1^p, the spin structure functions of the neutron and proton, respectively [14]. HMC itself does not currently include a generator for elastic ρ^0 production. However, it is a means to study the background to the elastic ρ^0 signal: processes due to hard $\gamma^* - quark$ interactions and subsequent fragmentation. The section below will provide a general description of HMC and the fragmentation model.

A separate program (BMC) was available to simulate the generation of elastic ρ^0 mesons. It generated the final state kinematics of the scattered positron and the two pions from the ρ^0 decay. Modifications to HMC allowed the output of this program to be used enabling these three particles to be tracked through the detector simulation. A brief description of this program will be given in Section 4.2 at the end of this chapter.

The reason for merging the BMC generator and the detector simulation in HMC is because the acceptance of the detector is limited and the elements of the ρ^0

spin density matrix are to be determined. For a three particle final state it is difficult to correct for the acceptance in the angular distributions analytically. It is especially difficult because the matrix elements that determine the distributions are not known in advance. The acceptance is modelled by generating elastic ρ^0 events weighted evenly in the angular distributions and using the detector simulation of HMC. Sometimes these simulated particles will not reach the electromagnetic calorimeter or are rejected when the criteria to select elastic ρ^0 events are applied. The particles from elastic ρ^0 production in the simulation and in the real physical events will have been subject to the same acceptance effects and can then be compared.

To determine the matrix elements, the simulated elastic ρ^0 events can then be weighted according to the equation that yields the angular distributions. The matrix elements that give the best fit to the distributions in the actual data are then the solution. The details of this procedure are found in Section 5.3.1.

4.1 The HERMES Monte Carlo

HMC is used is to model the background of elastic ρ^0 production. The events generated with this Monte Carlo do not include elastically produced ρ^0s. The actual data from the experiment, on the other hand, includes both elastically produced ρ^0s as well as background events due to hard $\gamma^* - quark$ interactions and subsequent fragmentation. The criteria to select those events with an elastic ρ^0 signal (described in Chapter 5) can be applied to the HMC events. The events that satisfy these criteria can then be said to represent the background of elastic ρ^0 production found in the experimental data. Another benefit of a Monte Carlo program is that the identity of the final state particles in the simulation are known.

4.1.1 DIS Generator

The first step in the generation of a DIS event is the calculation of the cross section for a hard γ^*-parton interaction. The kinematics of the scattered positron, quarks, and gluons are the result of this calculation. The distributions of the quarks and gluons in the nucleon are needed as input parameters. In the case of a polarized positron on a polarized target, the spin distributions of these particles are required as well.

The generator that produces the DIS final state in the polarized case is PEPSI [15, 16]. It is a modification of LEPTO [17], a generator for the case of unpolarized lepton-nucleon scattering. PEPSI employs polarized parton distributions to generate the required asymmetries simulating the spin structure function measurement. Except for small differences, the polarized and unpolarized cases are similar. The details regarding the polarized case will not be discussed further as they will not be revelvant for this analysis of elastic ρ^0 production.

There are three processes that can occur in a γ^*-parton interaction to lowest order in QCD and are shown in Figure 4.1. The first case (a) is a q-jet event where the virtual photon 'kicks out' a quark from the nucleon. The two remaining quarks of the nucleon is termed a *diquark*. The second possible case (b) is is that a $q\overline{q}$ pair can be produced in a γ^*-gluon event, also known as boson-gluon fusion. The last possibility (c) is for a gluon to be radiated in a γ^*-quark scattering event. The scattering processes in cases (a) and (c) do not have to involve a valence quark. Instead, the struck parton could be a sea quark.

The LEPTO generator uses the Lund string model [18] for fragmentation of these resulting states into hadrons. The simplest case is illustrated by considering a q and $\overline{q}$ travelling in a space of 1+1 (one space and one time) dimensions. A linear

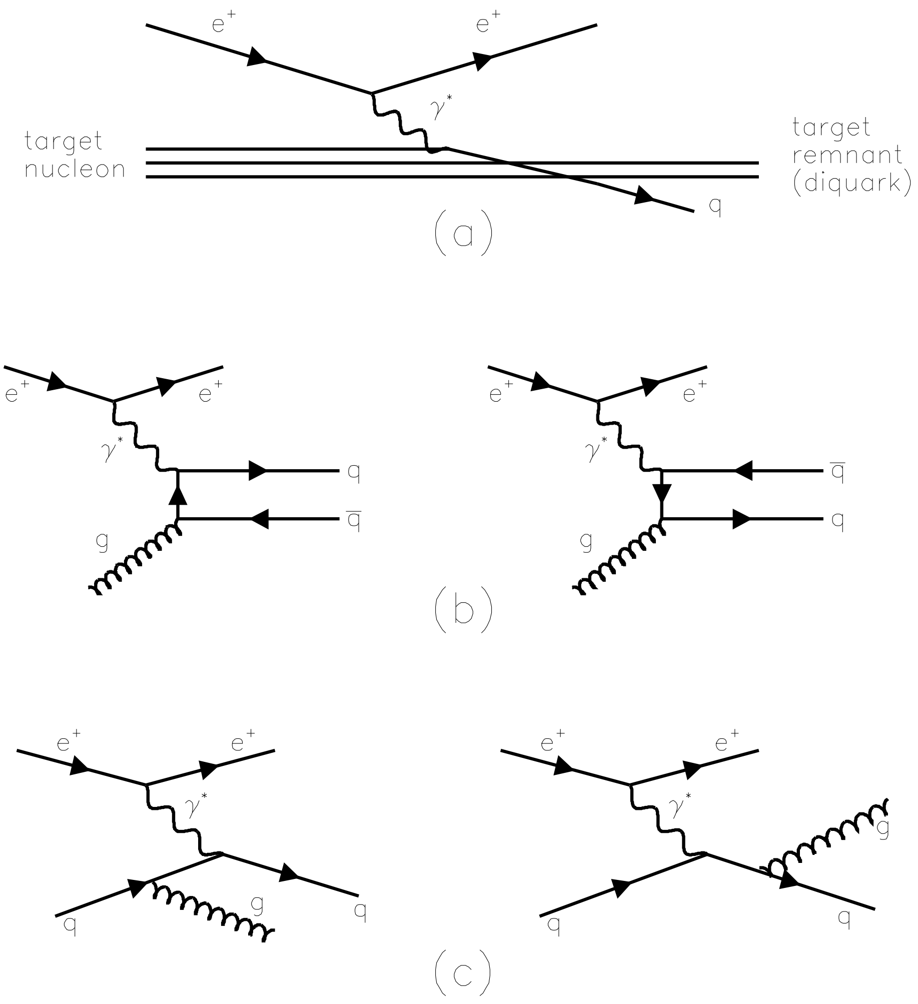

Figure 4.1: Virtual photon-target scattering processes used in HMC. The virtual photon can kick out a quark from the nucleon (a). Quark-antiquark pairs can be created in boson-gluon fusion (b). Gluons can also be emitted from the struck quark (c). (The lines for the non-interacting quarks are not shown in (b) and (c).)

color field (string) is created between them as a consequence of quark confinement. If p_1 (p_2) and x_1 (x_2) are the momentum of the quark (antiquark), the energy of this field is given by the Hamiltonian

$$\mathrm{H} = |p_1|^2 + |p_2|^2 + \kappa|x_1 - x_2| \tag{4.1}$$

if the quarks are assumed to be massless. The strength of the field is given by κ and has an approximate value of $\kappa = 1$ GeV/fm. Let q_0 and $\overline{q_0}$ designate the original quarks in the system. Given that the color field has sufficient energy, quark-antiquark pairs ($q_1\overline{q_1}$) are created (see Figure 4.2(a)). The quark, q_1, will join with the original antiquark $\overline{q_0}$, and $\overline{q_1}$ will become paired with the quark, q_0, and now represent two systems similar to the original. The energy is divided between the two systems such that if one is given a fraction, z ($0 \leq z \leq 1$), of the original energy, the other obtains an energy fraction $1 - z$. Constraints are placed on the fraction z to obtain the correct mass for the particular hadron being produced. Given enough energy, this process is repeated until the final hadronic state is produced. It is also possible for a diquark-antidiquark pair to be created (Figure 4.2(b)) and the same iterative procedure is applied. In this case, baryons (and antibaryons) are created in the hadronization process.

The creation of quark-antiquark pairs is modelled after the quantum mechanical tunneling mechanism. In this way, the resulting systems of hadrons are given transverse momentum. As well, the production of heavier quark pairs is naturally supressed. The ratio of the probabilities in creating the four lightest quarks pairs is

$$d{:}u{:}s{:}c \quad (1 : 1 : \frac{1}{3} : 10^{-11}). \tag{4.2}$$

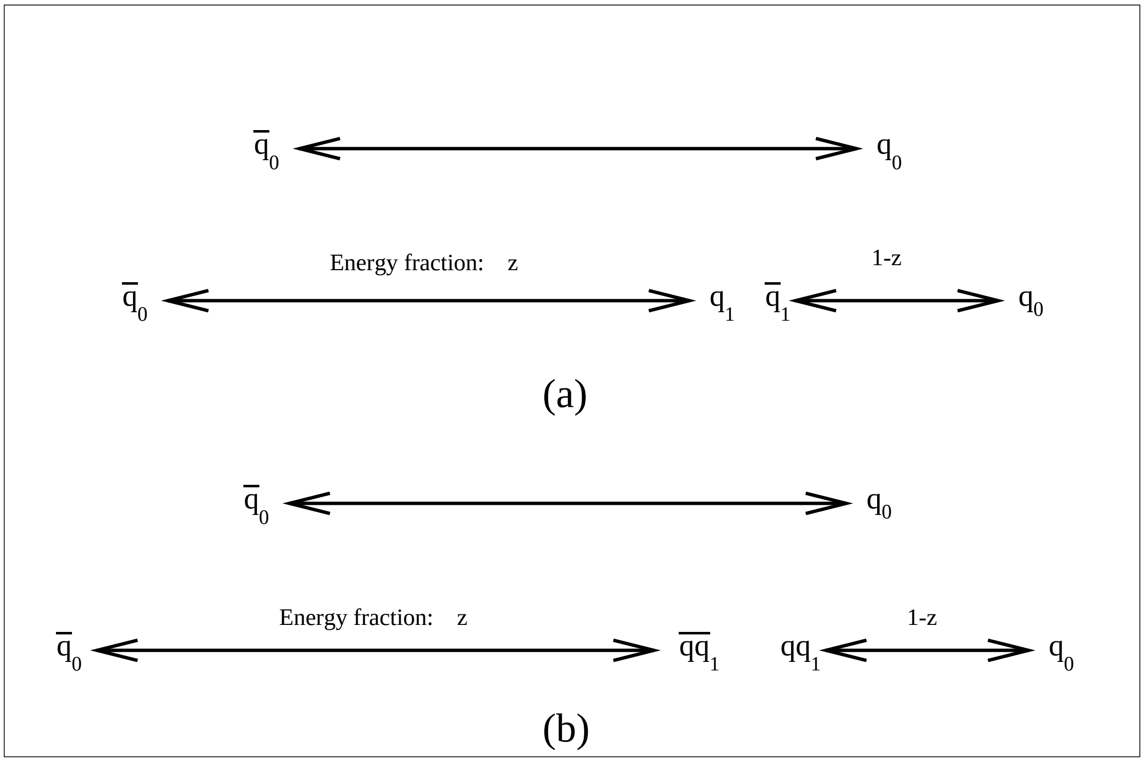

Figure 4.2: The creation of quark-antiquark (a) and diquark-antidiquark (b) pairs in a color field.

The b and t quarks are very massive so $t\overline{t}$ and $b\overline{b}$ pair production is neglected.

As listed above, there are several possible scenarios for the γ^*-parton interaction in lepton-proton scattering. If the struck quark is a valence quark, a color string is stretched between the outgoing quark and the remaining diquark and the hadronization proceeds as described above. The production of $q\overline{q}$ pairs will leave the diquark with a quark to form a baryon as is required from baryon number conservation. The diquark is not a single entity, but may also have a color field stretched between its constituent quarks. Pair production in this case would result in the formation of a hadron and still leave a diquark for a baryon to be produced.

A sea quark (q_s) will always have a corresponding antiquark ($\overline{q}_s$). If the interacting quark is a sea quark or antiquark, a color string is stretched between the q_s and $\overline{q}_s$ and hadronization proceeds as described above.

For the case of boson-gluon fusion, the quark-antiquark pair from $\gamma^* g \rightarrow q\overline{q}$ form a color string. In addition, a separate string is formed by splitting the target remnant into a quark-diquark pair. The hadronization for each system proceeds as described above.

The last case is of the struck quark radiating a gluon. Gluons are represented as 'kinks' on the string. The string breaks on either side of the kink, each break producing a $q\overline{q}$ pair such that the resulting hadron has the correct physical mass.

Once the hadronization procedure above is completed, the momentum of the resulting particles is established. The final state particles are then tracked through the simulation of the spectrometer as described in the next section.

4.1.2 Detector Simulation

Once the nature of and kinematics of the final state are established, they are tracked through the spectrometer. To accomplish this task, HMC uses a software package called GEANT [19]. With a model of the detector, the acceptance and individual detector responses are simulated. The DIS generator and detector simulation together provide a way of understanding the spectrometer and physics of the HERMES experiment.

The model of the spectrometer is an important part of the simulation. Each part of the detector is defined as a *volume* which is a basic geometrical shape with a material, or a mixture of materials associated with it. The definition of the material dictates the way the particles are to be tracked through it. Different volumes are built up to construct the facsimile of the detector. Another aspect of the model is that the magnetic field is also specified. Paths of charged particles are deflected in the magnetic field as they are tracked in the simulation.

Particles are tracked through the spectrometer in short steps. The length of the steps are a function of particle type, the material the particle is travelling through, and how much the track is bent when it is traversing a magnetic field. Step length is also limited close to boundaries between volumes. In each step, the program checks to see if the particle was scattered, decayed, lost energy (via Bremsstrahlung or ionization), underwent a nuclear reaction, etc. Tracking of a particle is abandoned if it decays or leaves the boundaries of the 'mother' volume which contains the entire spectrometer. Tracking is also discontinued if its energy falls below a set value. This is important as GEANT is claimed to accurately simulate physical processes for energies above ~ 1 keV. Any additional particles that are created (by decays or Bremsstrahlung, for example) are also tracked in a similar way.

The volumes that correspond to the active parts of the detectors are known as sensitive volumes. A *hit* is recorded whenever a particle travels through such a volume. The program keeps track of the energy deposited in the sensitive volume as well as the entrance and exit points of the particle. Each detector has its own special routine to simulate the final ADC or TDC response. Detector efficiencies and resolutions are also included in the simulation.

In general, the data and HMC output are comparable. A comparison in the context of event selection and topologies will be made in Section 5.1.4.

4.2 Diffractive ρ^0 Generator

A physics generator known as the Baby Monte Carlo (BMC) has been written* to model diffractive ρ^0 production in the kinematic realm of HERMES. It provides the kinematics of the final state positron and pions, optionally taking into account the angular dependancies that are being investigated. The details regarding the generator can be found in [20].

Modifications to the official HMC were made so that events from this generator can be read in allowing the positron and pions to be tracked through the spectrometer. A picture of an elastic ρ^0 event in the detector simulation is shown in Figure 4.3. More details on how these events were used will be presented in the analysis (Chapter 5).

*Author: T.G. O'Neill, Argonne National Laboratory, Argonne, Illinois 60439, USA.

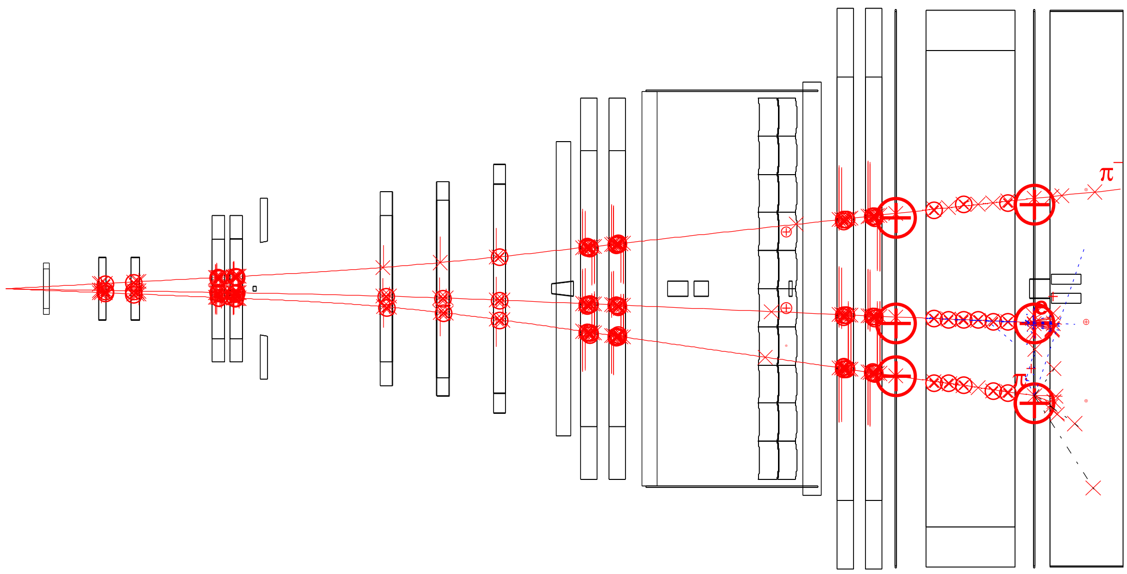

Figure 4.3: Example of an elastic ρ^0 event in the detector simulation (top view). The tracks from top to bottom are from the π^-, e^+, and π^+, respectively.

CHAPTER 5

Analysis

The fact that the ρ^0 meson decays most of the time into two charged particles makes the reconstruction of its momentum and mass relatively easy. With an appropriate set of cuts, a signal from elastically produced ρ^0 mesons can be isolated. The extraction and analysis of the elastic ρ^0 signal will be presented in this chapter. The major issues of concern will be the background contribution from DIS/fragmentation processes as well as the acceptance of the spectrometer. The size of the background will be determined with the HERMES Monte Carlo and the issue of the acceptance will be dealt with when the method for determining the spin density matrix elements is presented.

5.1 Extraction of the ρ^0 Meson Sample

5.1.1 Event Topology and PID

The basic requirement for an event to be considered in the analysis is that three tracks must be present – one from the scattered positron and two from oppositely charged hadrons. The final target state remains undetected. The PID detectors are used to differentiate between positrons(electrons) and hadrons. Particle tracks that satisfied the following cuts were identified as positrons:

$$\text{charge : positive} \tag{5.1}$$

$$E_{pre} > 0.01 \ \text{GeV} \tag{5.2}$$

$$N_{cer} > 0.2 \ \text{photoelectrons} \tag{5.3}$$

$$E_{cal}/P > 0.6 \tag{5.4}$$

where E_{pre} and E_{cal} are the energies deposited in the preshower and calorimeter, respectively. N_{cer} is the number of collected photoelectrons in the Cerenkov, and P is the reconstructed momentum of the particle. Tracks that are not identified as positrons are considered hadrons with the appropriate charge as determined from their path through the magnet. These are the same cuts as used in [21]. They are not very restrictive and allow for a large sample of candidate events to be identified.

Some standard cuts (the so-called fiducial cuts) that are used in the analysis of HERMES data are also employed [22]. The following cuts were made:

- to ensure a well defined acceptance edge near the shielding plate in the magnet:

$$\mid \arctan(p_y/p_z) \mid > 0.040 \qquad \text{(all particles)} \tag{5.5}$$

- z-position of vertex:

$$\mid z \ \text{of vertex position} \mid < 30 \ \text{cm} \quad \text{(positron only)} \tag{5.6}$$

- to make sure the positron is away from the calorimeter edge:

$$\mid x \ \text{position in calorimeter} \mid < 175 \ \text{cm} \qquad \text{(positron only)} \tag{5.7}$$

$$\mid y \ \text{position in calorimeter} \mid > 30 \ \text{cm} \qquad \text{(positron only)} \tag{5.8}$$

5.1.2 Kinematical Cuts

The data largely contains events arising from DIS/fragmentation processes. The objective is to define cuts that 1) maximize the number of elastically produced ρ^0 mesons while at the same time 2) allow events from HMC to be used in the analysis of the background.

Events were selected that satisified

$$Q^2 > 0.5 \text{ GeV}^2 \tag{5.9}$$

$$W^2 > 4.0 \text{ GeV}^2 \tag{5.10}$$

$$y < 0.85\,. \tag{5.11}$$

The cuts in Q^2 and W^2 are to select DIS events and were used as cuts when the HMC events used to investigate the background were generated. The cut in y ensures that the track associated with the positron had enough energy to generate a trigger. All events (data and Monte Carlo) satisfy these criteria unless otherwise stated.

The above variables are used to select events in kinematical regions consistent with deep inelastic scattering. To isolate the elastically produced ρ^0 mesons, some additional variables are needed. The most obvious variable to use is the invariant mass of the 2-pion system. The momentum of the detected hadrons shall be denoted as p_{h^+} and p_{h^-} because it can be difficult in practice to determine whether a given hadron is in fact a pion or other hadron. The invariant mass of the 2-hadron system can only be found if the mass of the hadrons are known. In this case, the hadrons are assumed to be pions, and the resulting expression for the invariant mass, $M_{2\pi}$, becomes

$$M_{2\pi} = \sqrt{(E_{\pi^+} + E_{\pi^-})^2 - \mid \vec{p}_{h^+} + \vec{p}_{h^-} \mid^2} \tag{5.12}$$

where

$$E_{\pi^\pm} = \sqrt{\mid \vec{p}_{h^\pm} \mid^2 + m_{\pi^\pm}^2}. \tag{5.13}$$

The target remnant(s) are not detected, but the invariant mass of the undetected state can be calculated and compared to the original target mass to determine if elastic production did indeed take place. Therefore limits will be placed on the variable ΔE which is defined in Chapter 2. The value for M_{targ} is taken to be the mass of the proton, $M_p = 0.938$ GeV. It is therefore expected that $\Delta E \approx 0$ GeV for incoherent, elastic ρ^0 production on a ^{3}He target. For coherent scattering, ΔE will be slightly positive because the M_{targ} that is used will be too small.

It was also stated in Chapter 2 that the elastic production of ρ^0 mesons occurs at low values of $|t|$. The cross section has a similar dependence on the related variable t'. This variable will therefore also be considered in the extraction of candidate ρ^0 events.

The optimum ranges in these variables to obtain a elastic ρ^0 signal will be determined using the HERMES Monte Carlo and the DIS generator. Before this determination, a comparison between the data and HMC events will be made.

5.1.3 Data Quality

The quality of the data depends on the conditions under which it was taken. Stable performance of the spectrometer and beam is required for reliable results to be obtained. Occasional problems with the data acquisition system, the positron beam, and detector components were experienced during data taking, and therefore a set of data quality criteria has been defined for the 1995 running period [22].

To make the large quantity of data managable, the data in a given fill was taken in short *runs* which represent around 6-10 minutes of data taking. The data in a given run is also subdivided into units called *bursts* which are ~ 10 s in length. A number of runs were deemed unusable based on logbook information. Other than this, it is on the burst level that data quality selection criteria is applied.

Events in bursts that had any of the following problems were not considered for analysis:

- Poor beam polarization or beam polarimeter problems.
- Trips in the high voltage supply for the front or back chambers. Trips are indicated by a low tracking efficiency. To reliably reject bursts with HV trips, the bursts previous to and immediately after a trip were also rejected.
- The data acquisition system had periods with a large dead-time in the first bursts of a run. The first three bursts in a run were therefore rejected.
- Poor TRD or Cerenkov performance.
- Zero hits for all channels in H1 or the preshower.
- The gains of the calorimeter and the preshower as determined by the GMS are different from their nominal values.

In some runs, the bursts frequently change from good states to bad states, or there is only a small fraction of good bursts that remain. In this case, these runs are also rejected.

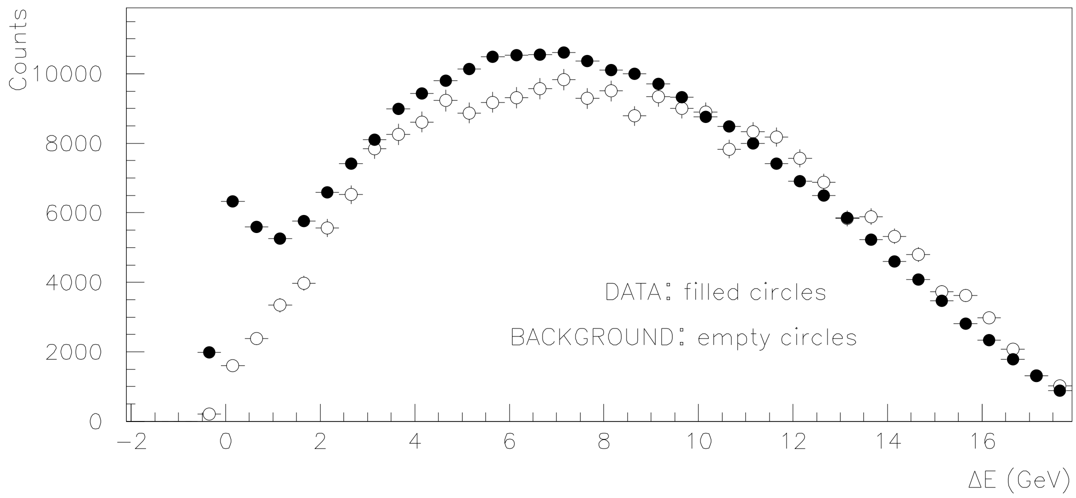

Figure 5.1: Comparison in ΔE of data and HMC background. The distributions are $(e^+h^+h^-)$ events satisfying the DIS cuts in Eqns.(5.9)–(5.11). The HMC background has been normalized to the data for $\Delta E > 3.9$ GeV.

5.1.4 Comparison of the HMC Background to the Data

A comparison between the data and HMC background events is necessary to ensure that the DIS generator and HMC is working properly and yielding reasonable results for the three-track $(e^+h^+h^-)$ events. The HMC events were generated at Max-Planck-Institut in Heidelberg, Germany and at the University of Alberta.

The distributions in ΔE for the data and HMC background should compare well in the region away from $\Delta E = 0$ GeV. A comparison is shown in Figure 5.1 where the cuts to select DIS events (Eqns.(5.9)–(5.11)) have been applied. The peak at $\Delta E = 0$ GeV in the data is due to the elastic production of ρ^0 mesons. The distributions are seen to compare reasonably well in the region at large ΔE.

The distributions in Q^2, ν, W^2, and $M_{2\pi}$ were also compared. The comparisons were also made for $\Delta E > 3.9$ GeV and are shown in Figure 5.2. The distributions agree very well as can be seen.

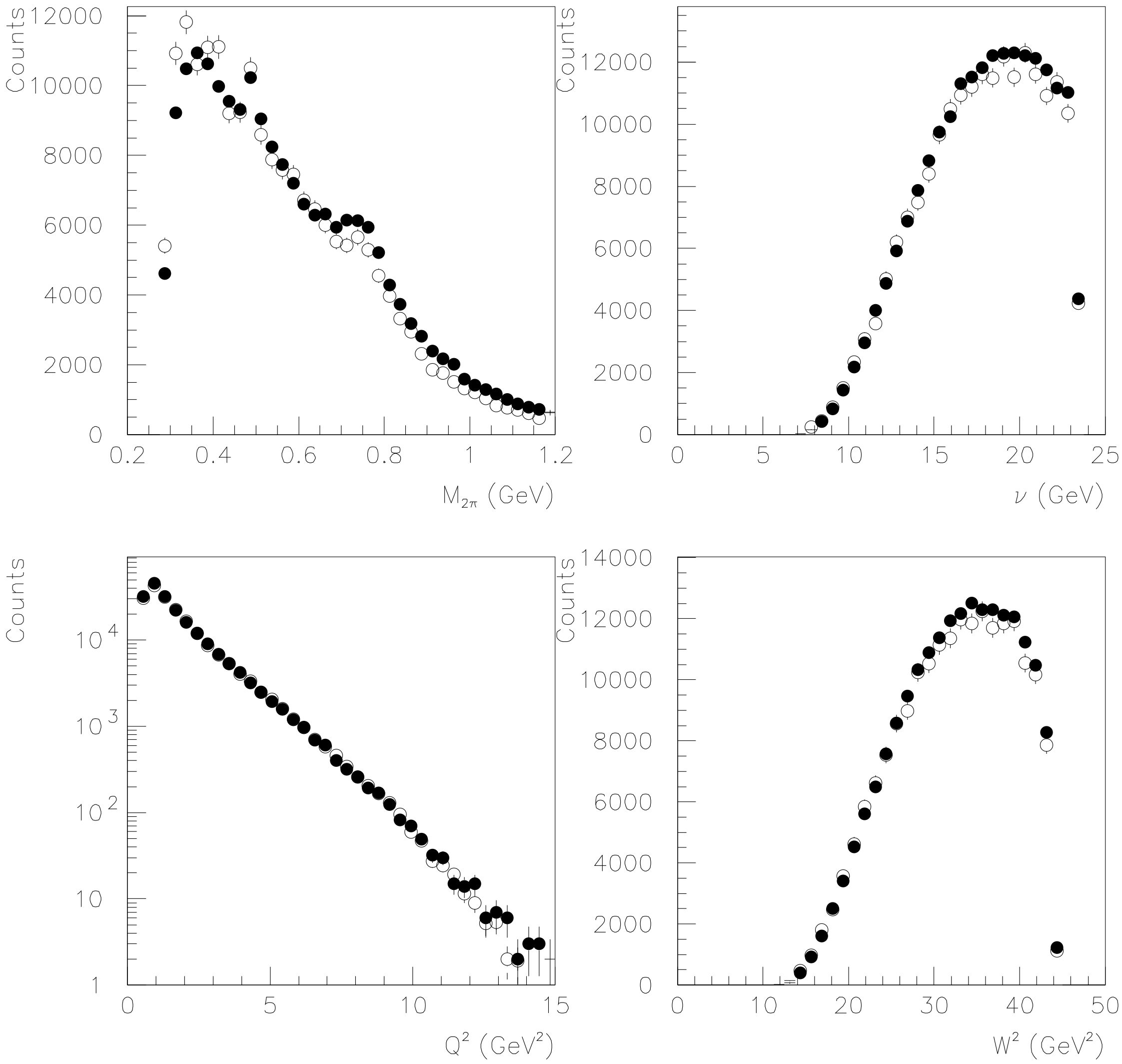

Figure 5.2: Comparison in Q^2, ν, W^2, and $M_{2\pi}$ of data (filled circles) and HMC background (empty circles). The distributions are $(e^+h^+h^-)$ events satisfying the DIS cuts in Eqns.(5.9)–(5.11). The HMC background has been normalized to the data for $\Delta E > 3.9$ GeV.

The comparison between the Monte Carlo and data is very good. There is no reason to believe that the distributions for HMC background events that lie below $\Delta E = 3.9$ GeV are not representative of the real background. This lends a confidence in the assumption that the background is modelled reasonably well in the Monte Carlo simulation of DIS events.

5.1.5 Cut Optimization

It was stated in Section 5.1.2 that the elastic production of ρ^0 mesons are characterized by $\Delta E \approx 0$ GeV, small values of $-t'$ (since $t' < 0$), and $M_{2\pi}$ around the value 0.770 GeV. To determine the optimal range of values in these variables to select interesting events, background events generated by the HERMES Monte Carlo were used.

The quantity chosen to be minimized in the optimization is the relative error in the elastic ρ^0 signal, $\delta S/S$. It is assumed that the signal is what remains after the Monte Carlo events are subtracted from the data. The relative error in the signal is given by the expression

$$\frac{\delta S}{S} = \frac{\sqrt{D + \alpha^2 \sum_i w_i^2}}{D - \alpha \sum_i w_i} \tag{5.14}$$

where w_i are the weights of the i Monte Carlo events used in the calculation. D is the number of data events used in the calculation and α is a normalization factor. The background is given by $\alpha \sum w_i$ and the normalization factor is found such that $D = \alpha \sum w_i$ at large ΔE ($\Delta E > 3.9$ GeV) where no elastic events occur.

The parameters $(\Delta E)_{cut}$, $(-t')_{cut}$, and $(M_{2\pi})_{cut}$ were varied so that HMC background and data events that satisfied

$$|\Delta E| < (\Delta E)_{cut} \tag{5.15}$$

$$|M_{2\pi} - 0.770 \text{ GeV}| < (M_{2\pi})_{cut} \tag{5.16}$$

$$-t' < (-t')_{cut} \tag{5.17}$$

were used to calculate (5.14).

Two analyses were performed so the results could be plotted and readily interpreted. In the first case $(\Delta E)_{cut}$ and $(M_{2\pi})_{cut}$ were varied and $(\Delta E)_{cut}$ and $(-t')_{cut}$ were varied for the second case. The resulting $\delta S/S$ as a function of these cuts are shown in Figures 5.3 and 5.4, respectively. As expected, the dependence on the cut in ΔE is the strongest; the optimum value in both cases is found to be $(\Delta E)_{cut} \simeq 0.6$ GeV. The corresponding dependence in $-t'$ and $M_{2\pi}$ is not as pronounced. The most probable explanation for this is that the background to the elastic ρ^0 signal also increases with $-t'$ and contains ρ^0 mesons arising from fragmentation processes. As determined from the figures, the most useful range that $(-t')_{cut}$ and $(M_{2\pi})_{cut}$ could be taken is

$$0.3 \text{ GeV}^2 < (-t')_{cut} < 0.5 \text{ GeV}^2 \tag{5.18}$$

$$0.13 \text{ GeV} < (M_{2\pi})_{cut} < 0.15 \text{ GeV}, \tag{5.19}$$

and the optimum values were taken to be

$$(-t')_{cut} = 0.4 \text{ GeV}^2 \tag{5.20}$$

$$(M_{2\pi})_{cut} = 0.14\text{GeV}. \tag{5.21}$$

The value for $\delta S/S$ is 0.022 for this set of cuts.

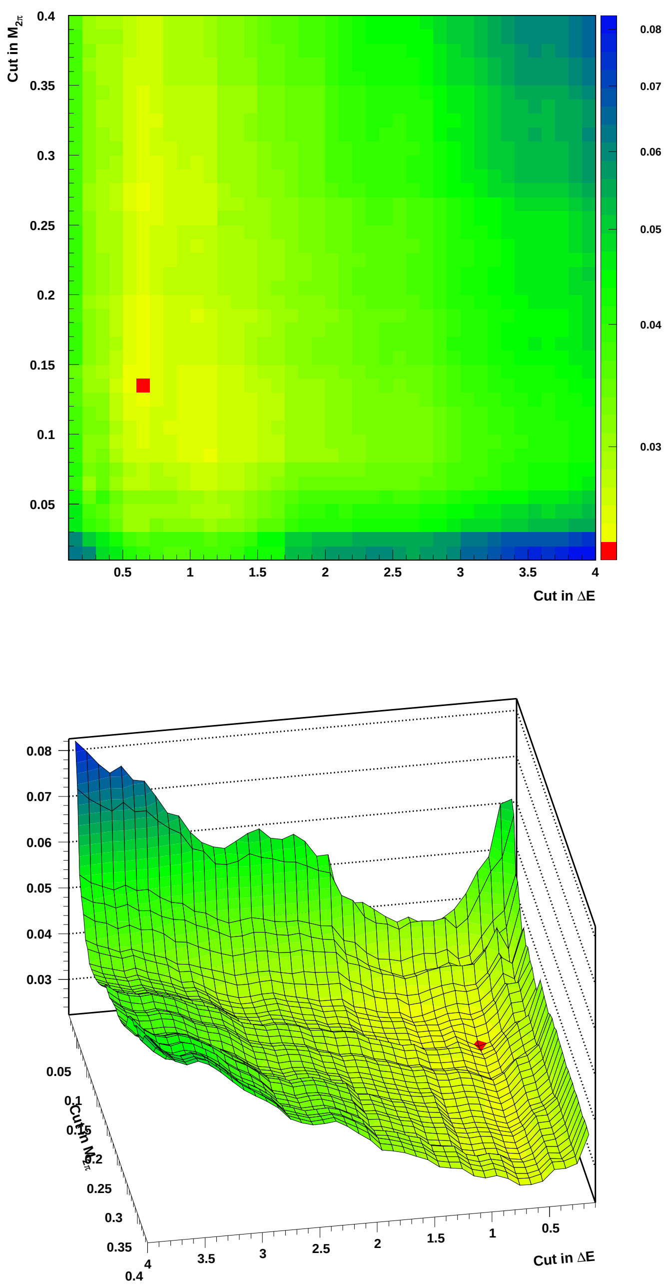

Figure 5.3: Relative error in the number of signal events for varying cuts of ΔE and $M_{2\pi}$.

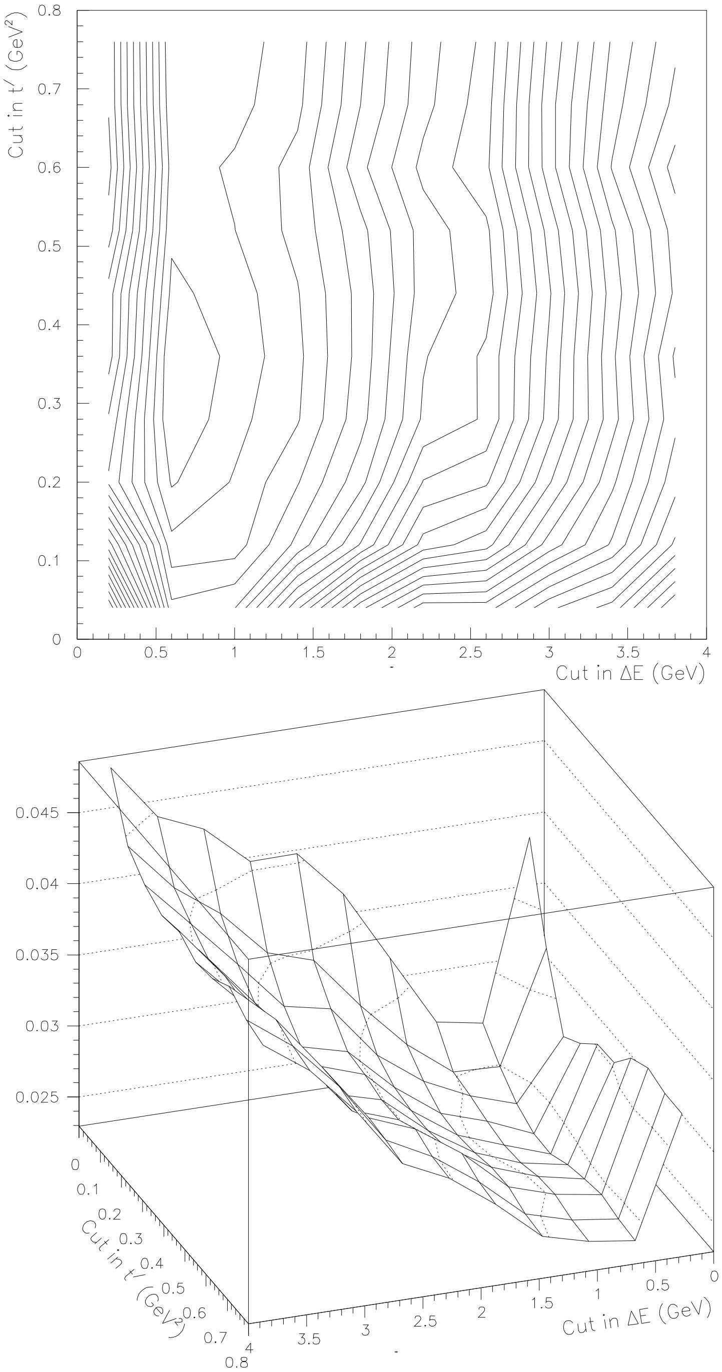

Figure 5.4: Relative error in the number of signal events for varying cuts of ΔE and $-t'$.

Using these results, the following cuts were also applied to obtain an elastic ρ^0 signal from the data:

$$\Delta E < 0.6 \text{ GeV} \tag{5.22}$$

$$-t' < 0.4 \text{ GeV}^2 \tag{5.23}$$

$$0.630 \text{ GeV} < M_{2\pi} < 0.910 \text{ GeV}. \tag{5.24}$$

The lower limit in the ΔE range was not necessary since there is no background for $\Delta E < -0.6$ GeV as shown in Figure 5.1.

The resulting mass spectrum for the elastic peak is shown in Fig. 5.5. The lines indicate the placement of the cut on $M_{2\pi}$ which defines the events to be used on the analysis of the angular distributions. There are 3091 events selected in this mass range. The size of the fragmentation background under this peak will be discussed in the next section.

The distribution in beam polarization of the selected events is shown in Figure 5.6. The average polarization is 55% with minimum and maximum values of 40% and 65%, respectively.

5.2 Background

The HERMES Monte Carlo can be used to study the background to the elastic ρ^0 signal that arises from fragmentation (i.e. hard γ^*-q processes.) This is believed to be the largest background contribution. The diffractive dissociation process also contributes, but it will be considered as part of the signal.

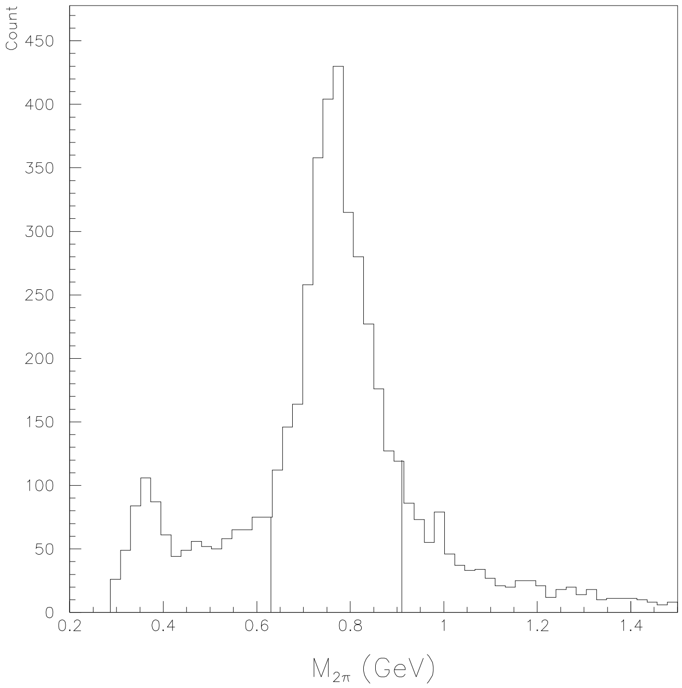

Figure 5.5: Invariant mass of the 2π system for selected ρ^0 events.

By using the distribution in ΔE, the amount of contamination in the elastic ρ^0 spectrum can be determined. The distributions in ΔE for the data and background HMC events are shown in Figure 5.7 where the criteria, Eqns.(5.23) and (5.24), to obtain an elastic ρ^0 signal are applied. The background distribution is normalized to the data at large ΔE, ($\Delta E > 3.9$ GeV) and compares very well with a $\chi^2/\text{ndf} = 35.2/29 = 1.2$. A peak occurs at $\Delta E \approx 0$ GeV in the data as expected, and the tail of the inelastic distribution lies underneath. The contribution of the background to the signal is found to be $\sim 8\%$ under the elastic peak when the chosen cut in ΔE, $\Delta E < 0.6$ GeV, is applied.

The number of HMC background events that satisfy the elastic ρ^0 selection criteria (61 events) is relatively small compared to the data. A large factor of 32.6 was used to normalize the HMC background to the data in Figure 5.7 and leads to a large uncertainty in the background subtraction. Fortunately, the size of the background is

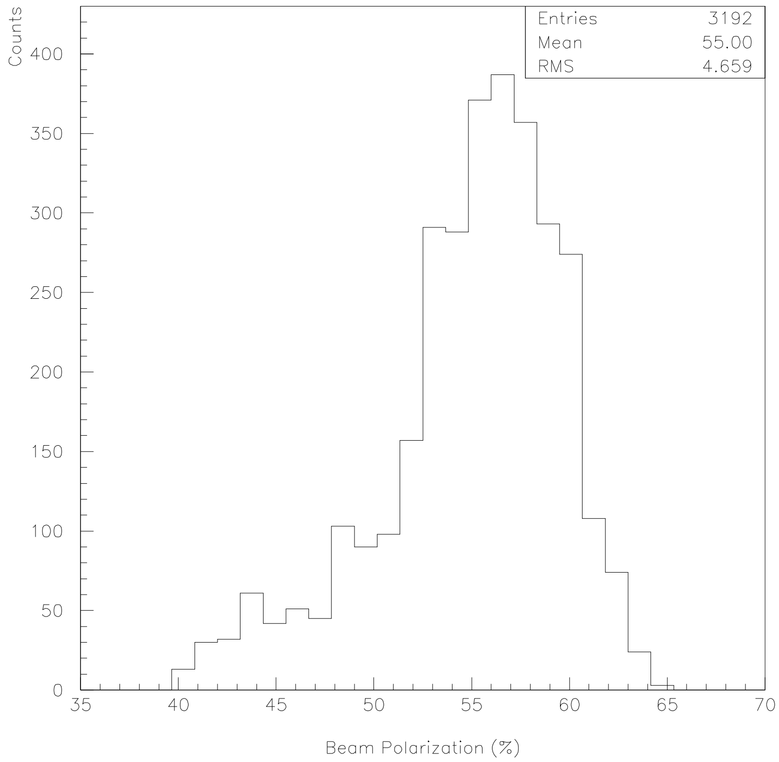

Figure 5.6: Beam polarization of selected ρ^0 events.

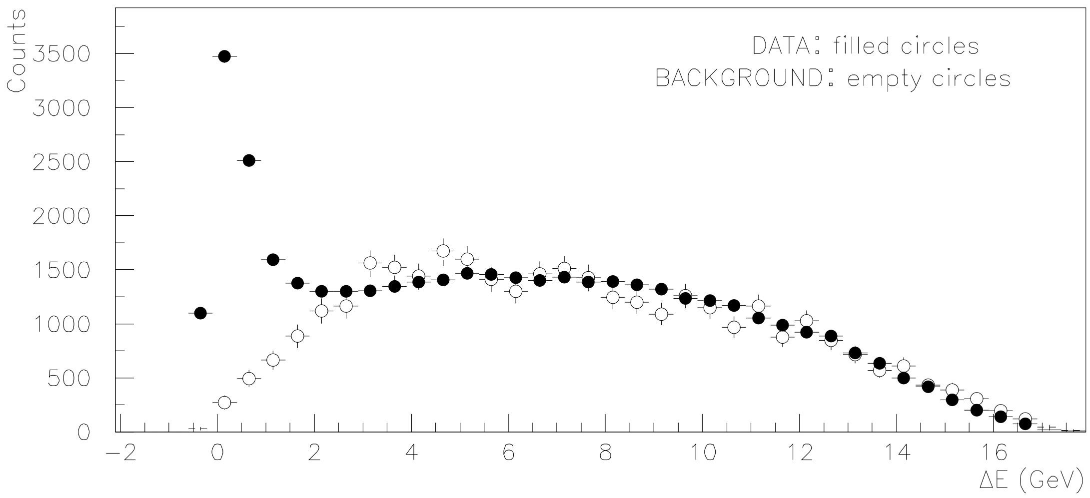

Figure 5.7: Distributions in ΔE for the data and HMC background with cuts in t' and $M_{2\pi}$ applied. The background has been normalized to the data.

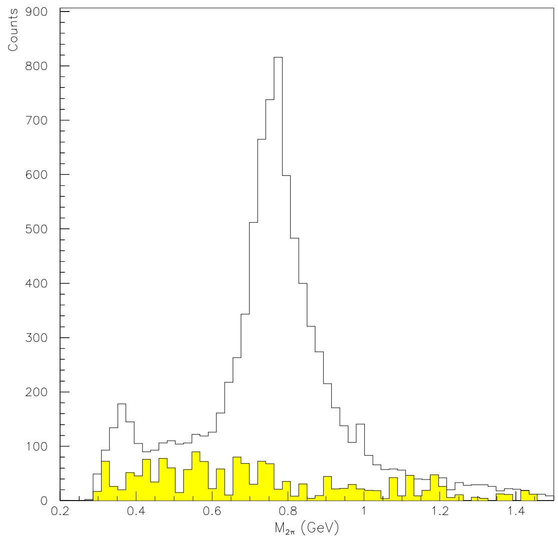

Figure 5.8: Reconstructed mass of the two hadron system with the expected contribution from the fragmentation background (shaded region).

small. See Figures 5.8 and 5.9 to see the resulting contribution to the mass spectrum and the angular distributions.

There is also a Q^2 dependence in R that must be taken into account. Therefore, the matrix elements r^{α}_{ik}, also have a dependence in Q^2. To accomodate this dependence, the data and reconstructed events were separated into 4 bins in Q^2 so that each bin has approximately the same number of data events. However, the number of background events are not evenly distributed as indicated in Table 5.1.

In all of the angular distributions, there are bins with zero counts. Two methods are employed to assign reasonable values and errors to these bins. Since the number of counts for background events is small for the lowest three bins in Q^2, the background is assumed to be uniform and the total counts were averaged over all bins in the angular distributions. In this way, the net number of background counts remains the same. For the bin largest in Q^2, values and errors for the angular distribution bins with zero counts are interpolated based on the counts of neighbouring

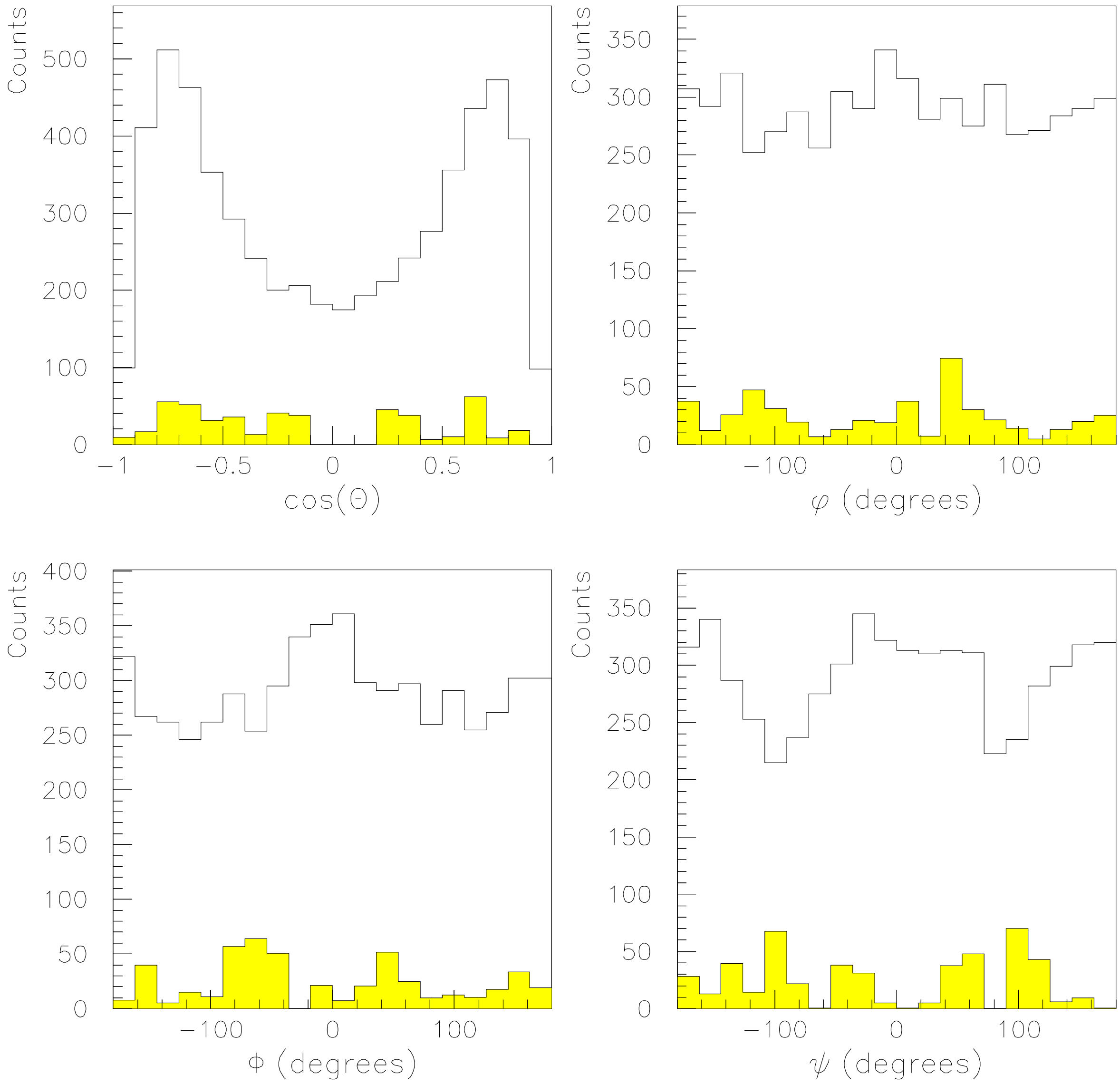

Figure 5.9: Angular distributions in $\cos\theta$, ϕ, Φ and ψ with the expected contribution from the fragmentation background (shaded region). No acceptance correction has been applied.

Bin No.	Range in Q^2 (GeV^2)	$< Q^2 >$ (GeV^2)	No. of background events	Percent contribution
1	0.50 – 0.95	0.80	2	4
2	0.95 – 1.30	1.13	5	7
3	1.30 – 1.96	1.60	7	6
4	1.96 – 10.0	2.75	47	13

Table 5.1: Definition of the bins in Q^2 and contribution of the background. All criteria to select elastic ρ^0 events have been applied.

bins.

It is of some interest to identify the type of events and particles that constitute the background. The universal identification of all hadrons as pions is assumed and is partly justified because most of the hadrons are in fact pions. However, the availabilty of HMC background events may give clues as to how the background may be reduced in the future.

The identity of each particle is given in the Monte Carlo. When the same cuts that were used to isolate the ρ^0 are applied, it is found that the scattered positron is always correctly identified. However, a number of kaons and protons make it into the background as seen in Table 5.2. The percentages given have the appropriate weights applied. According to the HERMES Monte Carlo, almost 50% of the background are $\pi^+\pi^-$ pairs and two-thirds of those are from a ρ^0 produced via framentation. The existence of a $\rho^0 \to \pi^+\pi^-$ background is not unexpected because a struck quark subsequently forming into a single ρ^0 will also appear at $\Delta E \approx 0$.

The other half of the hadronic background, according to HMC, consists of pairs which include one or more kaons or protons. The mass of the pion is assumed in the

Background Hadrons	%
$\pi^+\pi^-$ from ρ^0	30
$\pi^+\pi^-$ not from ρ^0	17
$p\pi^-$	22
K^+K^-	9
$p\overline{p}$	8
$K^+\pi^-$	2
π^+K^-	1

Table 5.2: Hadron pairs from HMC background satisfying ρ^0 selection criteria.

calculations of the kinematics and accounts of the inclusion of this type of fragmentation background because the wrong mass is used. The use of the Cerenkov detector and time-of-flight measurements to distinguish between pions and other hadrons at high and low momenta, respectively, may help to reduce this background in future studies.

There is a possibility that the fraction of protons in the background is too large. A large fraction of protons would be predicted if the DIS generator creates too many diquark–antidiquark pairs in the color field relative to the number of $q\overline{q}$ pairs. This effect has in fact been seen [23].

5.3 Determination of Matrix Elements

The main objective of this study is to determine the values of the remaining independent matrix elements when SCHC and natural parity exchange are assumed. The values of $R = \sigma_L/\sigma_T$ and the relative phase between the longitudinal and transverse helicity amplitudes are also to be found. If the fragmentation generator in HMC is assumed to give reasonable results for the generation of final states with multiple hadrons, then the background can be said to be understood and the other issue that must be addressed is the effect of the acceptance. This section will detail the method and present the values obtained for the above quantities.

5.3.1 Method

The angular distributions from the elastic ρ^0 signal are significantly affected by the acceptance of the spectrometer. An analytical determination of the acceptance effect on a 3-body final state and a simultaneous determination of the matrix elements which yield the real angular distributions is an extremely difficult task. A simpler, more elegant approach has been suggested [24] and was used here.

The determination is based on the fact that the spectrometer is modelled well in the Monte Carlo for the experiment. Particles generated with the elastic ρ^0 generator (BMC) and tracked through the spectrometer in the simulation will be subject to the same acceptance as real particles in the real spectrometer.

Events were generated in the BMC with *isotropic* angular distributions and were subject to the tracking and reconstruction in the HMC detector simulation. Due to the acceptance of the spectrometer, a number of events no longer had a 3-track coincidence after reconstruction and were excluded. As well, the same criteria to select elastic ρ^0 events in the data were applied to these events. More details on the reconstructed BMC events are provided in the next section.

The following matrix elements were determined: r^{04}_{00}, $\mathrm{Re}\, r^5_{10}$, and $\mathrm{Im}\, r^7_{10}$. The relationship $r^1_{1-1} = \frac{1}{2}(1 - r^{04}_{00})$ was also assumed. A set of values for the matrix elements were chosen and the reconstructed BMC events weighted according to the angular distribution in Eqn.(2.40). The polarization of the positron beam, P, was taken to be 55%. The resulting distributions were compared to the data in $\cos\theta$, ϕ, Φ, and ψ. The matrix elements were varied until differences between the distributions of the data and the reconstructed BMC events were at a minimum. This iterative procedure was performed with the MINUIT [25] computer program. The differences were quantified by the total χ^2 between all four distributions.

An analogous procedure was performed to determine R and the phase angle δ. In this case, Eqn.2.44 was used to weight the reconstructed BMC events.

5.3.2 Reconstructed BMC Events

The elastic ρ^0 events are generated with a t' dependence that goes like $e^{-b|t'|}$ where $b = 6$ GeV^{-2} which corresponds to incoherent scattering. The distributions in the angles $\cos\theta$, ϕ and Φ were generated isotropically with no correlations between them. Table 5.3 defines the domain in each Q^2 bin and the number of reconstructed BMC events in each bin. The number of elastic ρ^0 events found in the data is also given.

It is possible for bremsstrahlung to be radiated and the reconstructed Q^2 of the event to be less that the real value. The events are binned according to the reconstructed Q^2, but events were generated with a larger upper bound in Q^2 to allow events to radiate down and be accepted into the correct bin.

The vertex for each event was generated along the beam in the target cell with $x, y = 0$ cm and a distribution in the z-direction according to the gas density profile. The vertex distributions for the z-direction are shown on the left in Figure 5.10. The distribution for the lowest Q^2 bin is somewhat asymmetric because the positron is

Bin No.	Range in Q^2 (GeV^2)	$< Q^2 >$ (GeV^2)	No. of reconstructed BMC events	No. of recontructed data events
1	0.50 – 0.95	0.80	7233	621
2	0.95 – 1.30	1.13	11201	816
3	1.30 – 1.96	1.60	10009	827
4	1.96 – 10.0	2.75	11702	827

Table 5.3: Population of the bins in Q^2 for reconstructed BMC and data events. All criteria to select elastic ρ^0 events have been applied.

scattered into a much smaller angle and has less chance of reaching the calorimeter unless the interaction is farther back. The positions of the positron hits in the calorimeter form an annulus and are shown in the right hand side of Figure 5.10. The acceptance edge due to the shielding plate in the magnet has the greatest effect for the lowest Q^2 bin. The fiducial cuts described in Section 5.1.1 have been applied to all bins in these events and the data to provide identical acceptance edges.

The events were also generated such that the minimum momentum of the pions was 1 GeV. The hadrons in the data and HMC background events were therefore also subjected to the same cut on the momentum.

5.3.3 Results

The matrix elements r^{04}_{00}, $\mathrm{Re}\, r^{5}_{10}$, and $\mathrm{Im}\, r^{7}_{10}$ were found by the method as discussed in Section 5.3.1. The best values for these matrix elements are listed in Table 5.4.

Figure 5.11 shows the values for r^{04}_{00} in relation to a similar analysis on the HERMES 1995 ^{3}He data [26] by J.E. Belz. Measurements from E665 [27] and ZEUS [28], [29] are shown for comparison. The agreement between the HERMES analyses diverges for the lowest value of Q^2. There are some differences between the

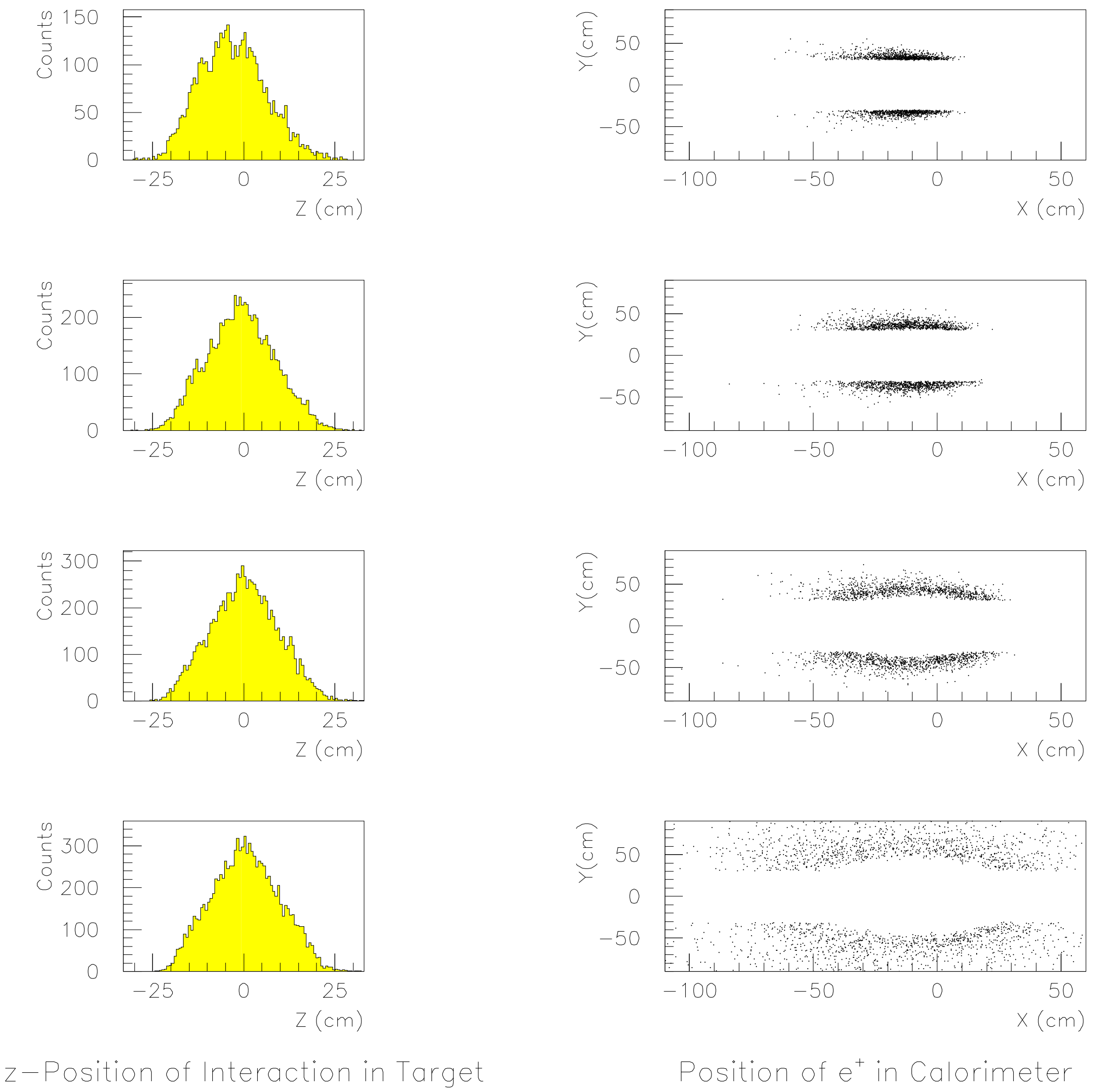

Figure 5.10: Vertex distributions and calorimeter position of the scattered positron. The four Q^2 bins (1–4) are shown with Q^2 increasing from the top to the bottom of the page.

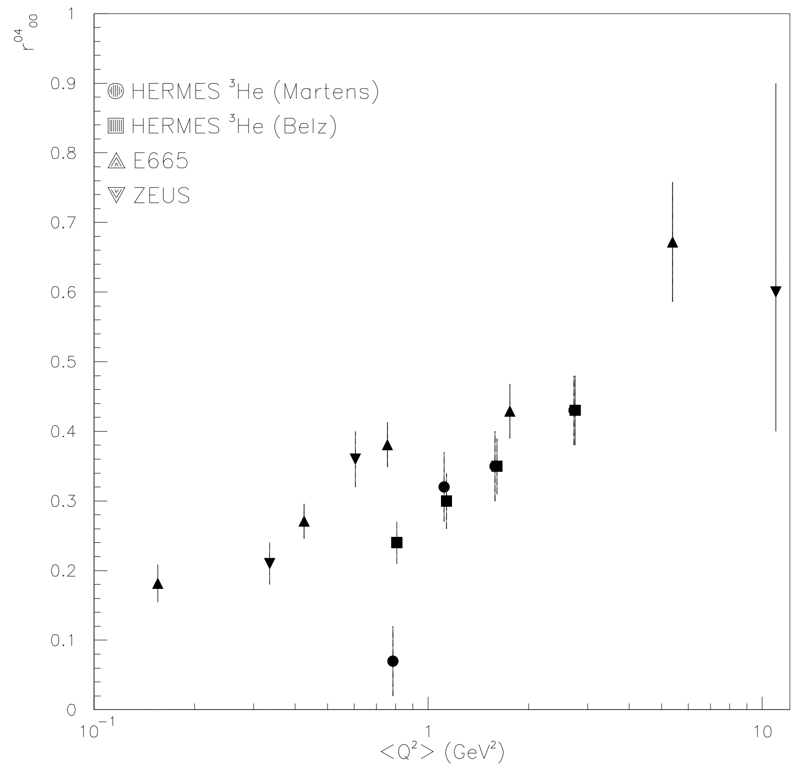

Figure 5.11: The matrix element r^{04}_{00} as a function of Q^2. The results from other experiments are shown for comparison.

analyses which are discussed below, but the reason for this disagreement is unclear.

The quoted errors are from the minimization procedure and do not include systematical uncertainties. A study of the systematic errors [26] revealed that the largest errors arise from uncertainties in the detector alignment. The errors will be largest for the lower range in Q^2 due to the limited acceptance of the spectrometer which is apparent in Figure 5.10. It should therefore be kept in mind that the errors in the measurements are larger than stated.

The best values for R and δ as determined by the method in Section 5.3.1 are found in Table 5.5. Figure 5.12 shows the values for R with other measurements for comparison. The values that are obtained agree well with [26] and with the other

$< Q^2 >$	0.80 GeV^2	1.13 GeV^2	1.60 GeV^2	2.75 GeV^2
r_{00}^{04}	0.07±0.05	0.32±0.05	0.35±0.05	0.43±0.05
$\mathrm{Re}\, r_{10}^{5}$	0.22±0.03	0.18±0.03	0.25±0.04	0.32±0.11
$\mathrm{Im}\, r_{10}^{7}$	-0.07±0.20	0.41±0.59	0.07±0.86	1.28±0.55
χ^2	85	93	123	76
ndf	80	80	80	80

Table 5.4: The optimal values for the matrix elements r_{00}^{04}, $\mathrm{Re}\, r_{10}^{5}$, and $\mathrm{Im}\, r_{10}^{7}$.

$< Q^2 >$	0.80 GeV^2	1.13 GeV^2	1.60 GeV^2	2.75 GeV^2
R	0.26±0.06	0.60±0.12	0.77±0.12	1.19±0.19
δ	0.00±0.26	0.20±0.69	0.00±0.38	0.42±0.55
χ^2	94	92	124	81
ndf	80	80	80	80

Table 5.5: The measured values for R and δ assuming SCHC and natural parity exchange.

experiments. The value of R measured by H1 was obtained from [30].

In most measurements, the method usually used for determining R is from the relation [27]

$$R = \frac{1}{\epsilon} \frac{r_{00}^{04}}{1 - r_{00}^{04}}. \tag{5.25}$$

The method that has been used here determines R independently of r_{00}^{04}. Both R and r_{00}^{04} increase with Q^2 which consistently indicates that longitudinally polarized ρ^0 mesons are preferentially produced at high Q^2.

Figure 5.13 shows the measured values of δ as a function of Q^2. These values are very close to zero and indicates that the relative phase between the amplitudes

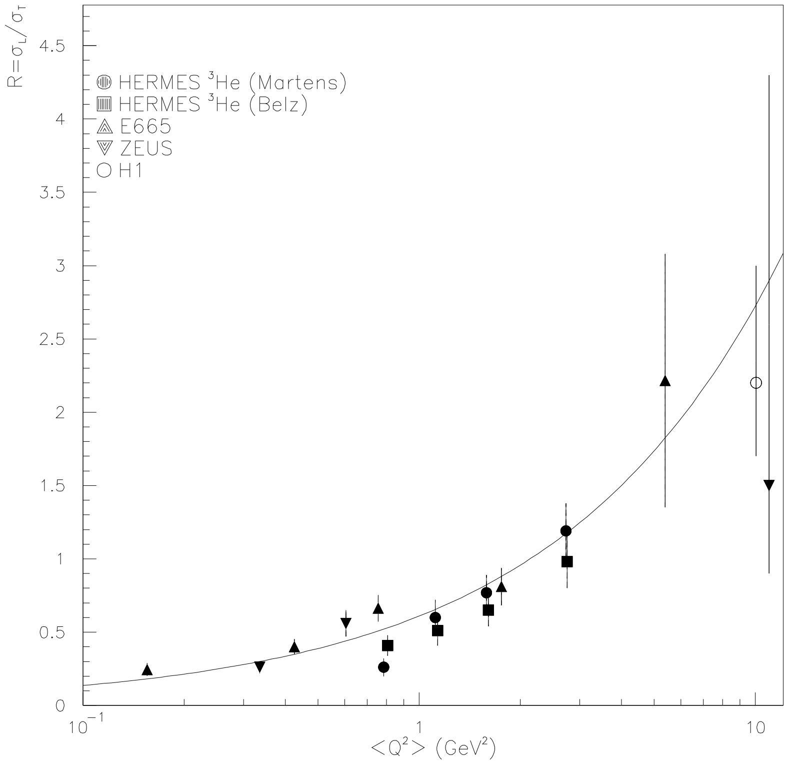

Figure 5.12: The ratio $R = \sigma_L/\sigma_T$ as a function of Q^2. The solid line is a fit to a set of world data [26].

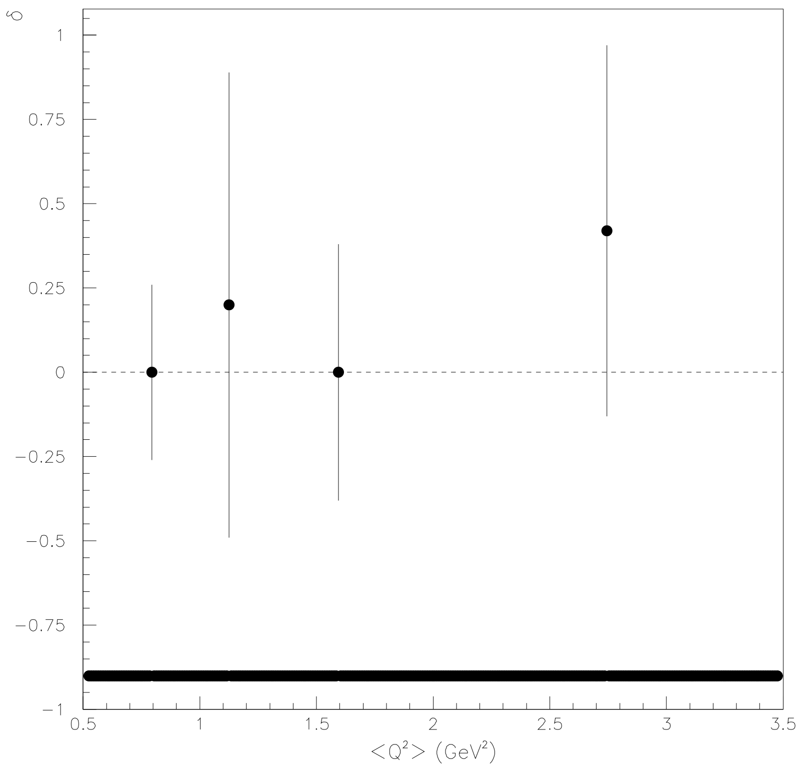

Figure 5.13: The phase angle δ as a function of Q^2.

$T_{0\frac{1}{2}0\frac{1}{2}}$ and $T_{1\frac{1}{2}1\frac{1}{2}}$ is small or zero. A result of zero for δ means that there is maximal constructive interference between the amplitudes to produce longitudinally and transversely polarized ρ^0 mesons.

Except for the largest bin in Q^2, the values obtained for $\mathrm{Im}\, r^7_{10}$ are also small which is consistent with the measured values of δ. The relationship between $\mathrm{Im}\, r^7_{10}$ and δ is given by

$$\mathrm{Im}\, r^7_{10} = \sqrt{\frac{R}{8}} \frac{\sin\delta}{1+\epsilon R}. \tag{5.26}$$

Since ϵ is not constant and is used in the calculation of the weight of each BMC event, it is difficult to determine whether $\mathrm{Re}\, r^5_{10}$ is consistent with δ according to a similar

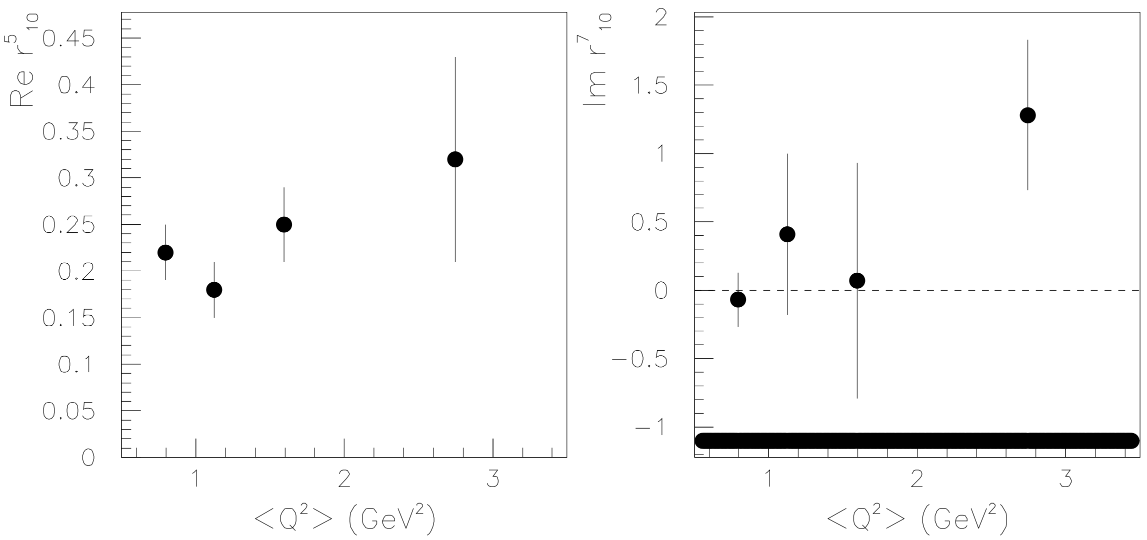

Figure 5.14: The values of $\mathrm{Re}\, r^5_{10}$ and $\mathrm{Im}\, r^7_{10}$ as a function of Q^2.

relationship

$$\mathrm{Re}\, r^5_{10} = \sqrt{\frac{R}{8}} \frac{\cos\delta}{1+\epsilon R}. \tag{5.27}$$

Figure 5.14 shows the values of $\mathrm{Re}\, r^5_{10}$ and $\mathrm{Im}\, r^7_{10}$ as a function of Q^2.

There are some differences between the analysis presented here and a similar analysis on the HERMES ^{3}He data [26]. Some of the major differences in this other study are:

- events are selected with $W^2 > 3.8$ GeV^2.
- a larger sample of elastic ρ^0 events are selected with $\Delta E < 0.7$ GeV and $-t' < 0.5$ GeV^2. The background will also be larger with these cuts.
- BMC events are weighted to account for the coherent distribution at low t'.
- SCHC was not assumed and a simultaneous determination of 8 matrix elements was performed.

The larger sample of ρ^0 events can lead to a more reliable result. A large uncertainty in the angular distributions can potentially lead the minimization routine to a meaningless result when the best fit between the data and BMC events is found.

To summarize, the value for R is found to be increasing with Q^2 as well as the value for r_{00}^{04}. This trend indicates that the analysis is consistent and more longitudinally polarized ρ^0 mesons are produced with increasing Q^2. The values for R agree well with the world data which together conflicts with the VDM prediction that R increases linearly with Q^2. The phase angle, δ, is small and consistent with zero suggesting that there is constructive interference between the amplitudes to produce transverse and longitudinally polarized ρ^0 mesons. The measured value for $\mathrm{Im}\, r_{10}^{7}$ is also consistent with small values of δ. Differences between this study and a similar analysis on the same data are most likely differences in analysis strategy. However, despite some discrepancies, the results in this study are relatively consistent.

CHAPTER 6

Conclusion

The spin density matrix elements were measured for elastically produced ρ^0 mesons in a kinematic range of $0.5\ \mathrm{GeV}^2 \leq Q^2 \leq 4\ \mathrm{GeV}^2$. The data was taken in 1995 using 27.5 GeV polarized positrons on a target of ^{3}He gas in the HERMES experiment located at DESY in Hamburg, Germany. The assumption of s-channel helicity conservation and natural parity exchange was used in the analysis. The ratio of cross sections, $R = \sigma_L/\sigma_T$, for elastic ρ^0 production from longitudinally and transversely polarized virtual photons was also measured. As well, the phase angle, δ, between the amplitudes $T_{0\frac{1}{2}0\frac{1}{2}}$ and $T_{1\frac{1}{2}1\frac{1}{2}}$ was determined.

The matrix elements r^{04}_{00}, $\mathrm{Re}\, r^5_{10}$ and $\mathrm{Im}\, r^7_{10}$ were measured assuming SCHC and natural parity exchange. The values for r^{04}_{00} are lower than expected, but indicate a rising trend with increasing Q^2 which is consistent with the measurement of R. The measured values for R agree well with a similar analysis on the HERMES ^{3}He data and with values obtained in other experiments. The value for δ was found to be small and was consistent with zero and with the small values obtained for $\mathrm{Im}\, r^7_{10}$.

In general, the results of this analysis were self-consistent despite the small number of ρ^0 mesons found. The analysis of the HERMES data from 1996-1997 promises to yield superior results. The data taken in this two year period will most certainly contain more ρ^0 mesons to study.

Bibliography

[1] T.H. Bauer, R.D. Spital, and D.R. Yennie. *The hadronic properties of the photon in high-energy interactions. Rev. Mod. Phys.*, 50(2):261–436, 1978.

[2] Particle Data Group. Review of Particle Physics. *Phys. Rev. D*, 54, 1996.

[3] K. Schilling and G. Wolf. *How to analyse vector-meson production in inelastic lepton scattering. Nucl. Phys.*, B61:381–413, 1973.

[4] F. Nichitiu. *Introduction to the Vector Meson.* Technical report, Laboratori Nazionali Di Frascati, Nov 1995. LNF–95/056 (P).

[5] D. DeSchepper et al. Submitted to Nucl. Inst. and Methods.

[6] HERMES Collaboration. *Technical Design Report*, 1993.

[7] K. Ackerstaff *et al.* (The HERMES Collaboration). *The HERMES Spectrometer.* To be submitted to Nucl. Inst. and Methods.

[8] W.R. Leo. *Techniques for Nuclear and Particle Physics Experiments.* Springer-Verlag, 1987.

[9] W. Wander. *Rekonstruktion hochenergetischer Streuereignisse im HERMES Experiment.* PhD thesis, University of Erlangen, 1996.

[10] J.D. Jackson. *Classical Electrodynamics, 2nd Edition.* John Wiley & Sons, 1975.

[11] R. Kaiser. *Measurement of the Spin Structure of the Neutron using Polarised Deep Inelastic Scattering.* PhD thesis, Simon Fraser University, 1997.

[12] M. Düren. *The HERMES Experiment: From the Design to the First Results*, July 1995. Habilitation Thesis (University Erlangen-Nürnberg), DESY Grey Report: DESY–HERMES 95–02.

[13] M. Düren et al. *The HERMES Monte Carlo Program*, 1995.

[14] K. Ackerstaff *et al.* (The HERMES Collaboration). *Measurement of the neutron spin structure function g_1^n with a polarized ^{3}He internal target. Phys. Lett. B*, 404:383–389, 1997.

[15] L. Mankiewicz, A. Schäfer, and M. Veltri. *PEPSI: A Monte Carlo generator for polarized leptoproduction. Comput. Phys. Commun.*, 71:305–318, 1992.

[16] M. Veltri et al. *PEPSI*, 1995. HERMES Collaboration.

[17] G. Ingelman. *LEPTO 6.5 - A Monte Carlo Generator for Deep Inelastic Lepton-Nucleon Scattering. DESY Note 96-057*, 1996.

[18] B. Andersson et al. *Parton Fragmentation and String Dynamics. Phys. Rep. Nos. 2 & 3*, 97:31, 1983.

[19] *GEANT: Detector Description and Simulation Tool.* CERN Program Library (Long Writeup W5013).

[20] M. Kolstein. PhD. Thesis, Nationaal Instituut voor Kernfysica, To be completed.

[21] T. G. O'Neill. *Improved Extraction of $A(e, e'\rho^0)$ Events at HERMES. HERMES Internal Note*, 1995.

[22] N. Akopov et al. *Determination of the 1995 Data Quality and the Extraction of the Spin Structure Function of the Neutron.* HERMES Internal Note: 97-007.

[23] H. Ihssen. Private Communication.

[24] J.E. Belz. Private Communication.

[25] *MINUIT: Function Minimization and Error Analysis.* CERN Program Library (Long Writeup D506).

[26] J.E. Belz. *Measurement of Tensor Polarization Observables in Exclusive Diffractive Electroproduction of Vector Mesons.* HERMES Internal Report, to be completed.

[27] M.R. Adams et al. *Diffractive production of ρ^0(770) mesons in muon-proton interactions at 470 GeV. Z. Phys.*, C(74):237–261, 1997.

[28] J.A. Crittenden. *Exclusive Production of Neutral Vector Mesons at the Electron-Proton Collider HERA.* DESY 97-068.

[29] M. Derrick et al. *Exclusive ρ^0 production in deep inelastic electron-proton scattering at HERA. Phys. Lett.*, B(356):601, 1995.

[30] The H1 Collaboration, DESY 96-023.

Appendix A

Spin Density Matrix Components: The Σ Matrices

The explicit expressions for the components of the spin density matrix of the virtual photon and ρ^0 are given here:

$$\Sigma^0 = \begin{bmatrix} 1 & 0 & 0 \\ 0 & 0 & 0 \\ 0 & 0 & 1 \end{bmatrix}; \quad \Sigma^1 = \begin{bmatrix} 0 & 0 & 1 \\ 0 & 0 & 0 \\ 1 & 0 & 0 \end{bmatrix}; \quad \Sigma^2 = \begin{bmatrix} 0 & 0 & -i \\ 0 & 0 & 0 \\ i & 0 & 0 \end{bmatrix};$$

$$\Sigma^3 = \begin{bmatrix} 1 & 0 & 0 \\ 0 & 0 & 0 \\ 0 & 0 & -1 \end{bmatrix}; \quad \Sigma^4 = 2\begin{bmatrix} 0 & 0 & 0 \\ 0 & 1 & 0 \\ 0 & 0 & 0 \end{bmatrix}; \quad \Sigma^5 = \frac{1}{\sqrt{2}}\begin{bmatrix} 0 & 1 & 0 \\ 1 & 0 & -1 \\ 0 & -1 & 0 \end{bmatrix};$$

$$\Sigma^6 = \frac{1}{\sqrt{2}}\begin{bmatrix} 0 & -i & 0 \\ i & 0 & i \\ 0 & -i & 0 \end{bmatrix}; \quad \Sigma^7 = \frac{1}{\sqrt{2}}\begin{bmatrix} 0 & 1 & 0 \\ 1 & 0 & 1 \\ 0 & 1 & 0 \end{bmatrix}; \quad \Sigma^8 = \frac{1}{\sqrt{2}}\begin{bmatrix} 0 & -i & 0 \\ i & 0 & -i \\ 0 & i & 0 \end{bmatrix} \tag{A.1}$$

Appendix B

Contribution to HERMES

I was involved with the HERMES experiment for the period May 1995 to March 1998. For the first four months, I was a summer student for the University of Alberta. In September 1995, I officially became a student in the Masters program. Some of the things I have contributed to the experiment are listed below in no particular order:

- Participation in data taking shifts for the running periods from 1995 through 1997.
- Responsible for Monte Carlo production at the University of Alberta. This task involved setting up, running, and maintaining the production.
- Installation of TRD electronics in the electronics trailer. The majority of this work involved making and testing cables.
- Performed a study for the Charm group. The positron in J/ψ production is scattered at small angles and travels down the beampipe. A chamber located at the position of the calorimeter to detect these positrons was proposed. The study entailed a computer simulation of the trajectory of low energy positrons through the magnetic field in the beam pipe.
- Pre-tested the preamplifiers for the Drift Vertex Chamber (DVC). The DVC was installed in 1996 to improve tracking performance between the target and

magnet. This task also included trouble-shooting and fixing defective preamplifiers.

- Wrote a trip detection program for offline data quality group. The program scans the slowcontrol data of the experiment to locate trips in the HV supply to the detector components. Previously, trips were detected by observing low detector efficiencies.